Check for updates

ADVANCED MATERIALS
www.advmat.de

Highly Sensitive Capacitive Pressure Sensors over a Wide Pressure Range Enabled by the Hybrid Responses of a Highly Porous Nanocomposite

*Kyoung-Ho Ha, Weiyi Zhang, Hongwoo Jang, Seungmin Kang, Liu Wang, Philip Tan, Hochul Hwang, and Nanshu Lu**

Past research aimed at increasing the sensitivity of capacitive pressure sensors has mostly focused on developing dielectric layers with surface/porous structures or higher dielectric constants. However, such strategies have only been effective in improving sensitivities at low pressure ranges (e.g., up to 3 kPa). To overcome this well-known obstacle, herein, a flexible hybrid-response pressure sensor (HRPS) composed of an electrically conductive porous nanocomposite (PNC) laminated with an ultrathin dielectric layer is devised. Using a nickel foam template, the PNC is fabricated with carbon nanotubes (CNTs)-doped Ecoflex to be 86% porous and electrically conductive. The PNC exhibits hybrid piezoresistive and piezocapacitive responses, resulting in significantly enhanced sensitivities (i.e., more than 400%) over wide pressure ranges, from 3.13 kPa^{-1} within 0–1 kPa to 0.43 kPa^{-1} within 30–50 kPa. The effect of the hybrid responses is differentiated from the effect of porosity or high dielectric constants by comparing the HRPS with its purely piezocapacitive counterparts. Fundamental understanding of the HRPS and the prediction of optimal CNT doping are achieved through simplified analytical models. The HRPS is able to measure pressures from as subtle as the temporal arterial pulse to as large as footsteps.

1. Introduction

Soft pressure sensors able to conform to curvilinear and even deformable surfaces are of increasing demand in emerging fields such as robotics, prosthetics, surgical tools, biometric sensors, and more.[1–3] For instance, advanced soft pressure sensors have been used for robot fingers handling delicate items,[4,5] artificial gloves distinguishing hand gestures,[6–8] tactile sensing,[9,10] noninvasive measurement of blood pressure,[11] and artificial vessels capable of detecting pulse waves.[12,13] Different applications correspond to different pressure ranges: subtle pressures below 1 kPa for ultrasensitive e-skin capturing soft touch[14] or palpating cardiovascular activity[15–17]; low pressures between 1 and 10 kPa for intrabody pressures[18,19] and pressures associated with daily activities (e.g., gentle manipulation of items)[20]; and high pressures of more than 10 kPa for blood pressure monitoring

K.-H. Ha
Department of Mechanical Engineering
University of Texas at Austin
Austin, TX 78712, USA

W. Zhang, L. Wang, H. Hwang
Department of Aerospace Engineering and Engineering Mechanics
University of Texas at Austin
Austin, TX 78712, USA

H. Jang
Texas Material Institute
University of Texas at Austin
Austin, TX 78712, USA

S. Kang
Department of Biomedical Engineering
University of Texas at Austin
Austin, TX 78712, USA

The ORCID identification number(s) for the author(s) of this article can be found under https://doi.org/10.1002/adma.202103320.

P. Tan
Department of Electrical and Computer Engineering
University of Texas at Austin
Austin, TX 78712, USA

N. Lu
Department of Aerospace Engineering and Engineering Mechanics
Department of Electrical and Computer Engineering
Department of Mechanical Engineering
Department of Biomedical Engineering
Texas Materials Institute
University of Texas at Austin
Austin, TX 78712, USA
E-mail: nanshulu@utexas.edu

DOI: 10.1002/adma.202103320

 © 2021 Wiley-VCH GmbH

devices[21] and the plantar pressure of body weight.[22] Sometimes, subtle pressures are even superimposed on high-pressure preloads, such as when pressure sensors are attached to target surfaces using a covering tape or incorporating pressure sensors under other wearable devices. For those applications, soft pressure sensors with high sensitivity throughout large pressure ranges are desired.

A variety of pressure-sensing mechanisms, including piezoresistive,[6,12,23–25] piezoelectric,[26–28] capacitive,[7,9,29–34] optical,[35,36] and ionic responses[37–39] have been explored. Under compression, the pressure-sensing materials generate changes in electrical resistance, voltage, capacitance, transmittance of light, or capacitance of an electric double layer, respectively. Piezoresistive pressure sensors have advantages of facile fabrication, simple structure, and readout circuits, but suffer from constant power consumption, large confounding temperature sensitivity, and hysteresis.[40–42] In contrast, piezoelectric sensors do not require input power but are only suitable for measuring dynamic pressures, such as pulses or vibrations.[40–42] Optical pressure sensors exhibit negligible signal drift but have limitations including complex setup, high power consumption, and signal alteration or attenuation due to bending or misalignment.[41,43] Ionic pressure sensors can be thin and transparent and possess enormous sensitivity due to the large capacitance change of the electrical double layer.[44,45] However, ionic sensors are less stable and/or biocompatible,[37] and require a threshold pressure for the ionogel and the electrode to make initial contact.[46–48]

In this research, we focus on capacitive pressure sensors due to their good repeatability, temperature independence, low power consumption, high spatial resolution, and suitability for large-area applications.[40–43] The sensitivity of capacitive pressure sensors mainly depends on the deformation of the dielectric material and is damped as the effective compressive modulus of the dielectric material increases with compression due to fixed boundaries.[49] In pursuit of higher sensitivity, recent research has focused on engineering the dielectric materials by adding air gaps and/or increasing their dielectric constants. Air gaps on the surface or inside of a dielectric material reduce the effective compressive modulus. Moreover, they enable the effective dielectric constant to increase with compression, as the volume fraction of air is replaced by solids with higher dielectric constants.[9] To incorporate air gaps in dielectric materials, strategies including micropatterned surfaces,[7,13,30,50–54] foams,[55–60] nanowire networks,[61,62] fabrics,[32,63] and spacing layers[29,33,64–66] have been employed. To enhance the effects of air gaps, methods such as coating and doping elastomers with high dielectric constant materials or conductive nanomaterials to achieve high dielectric constant composites have been explored.[58,60,62,67–71] However, these techniques for sensitivity enhancement were only effective over a small pressure range. The effects weaken as the air gaps diminish with compression. After extensive research in the past decade, the improvements of porosity and the dielectric constants have almost reached their limits. A fundamentally new strategy is needed to achieve capacitive pressure sensors with high sensitivity over wide ranges of pressure.

Herein, we report a novel capacitive pressure sensor employing the hybrid piezoresistive and piezocapacitive responses of a highly porous nanocomposite (PNC) to attain high sensitivity over a large pressure range (i.e., 3.13 kPa^{-1} within 0–1 kPa, 1.65 kPa^{-1} within 1–5 kPa, 1.16 kPa^{-1} within 5–10 kPa, 0.68 kPa^{-1} within 10–30 kPa, and 0.43 kPa^{-1} within 30–50 kPa). The PNC is composed of carbon nanotubes (CNT) and Ecoflex, and the ligaments of the PNC are electrically conductive due to adequate CNT doping. The PNC is 86% porous with an open cell structure that enables distributed parasitic capacitance. By adding an ultrathin solid insulating layer between the PNC and one side of the electrode, the whole device becomes capacitive. Under compression, the overall impedance response of the sensor is characterized by both the resistance and capacitance changes of the PNC. We therefore call it the hybrid-response pressure sensor (HRPS). Our HRPS is flexible and can be inexpensively fabricated without any vacuum facilities or microelectromechanical systems (MEMS) fabrication facilities such as cleanrooms. We show that although the sensitivity of our HRPS still decays with compression, the decay is quite mild compared with conventional capacitive pressure sensors; hence, high sensitivity can still be attained at large pressure. We also present an analysis based on simplified circuit models to fully determine the effects of each of the piezoresponses and moreover, to help determine the optimal CNT doping concentration. Finally, we demonstrate that our HRPS is able to measure pressures from as small as 0.07 Pa due to drosophila weight to as large as 125 kPa due to footsteps.

2. Experimental Methods and Results

2.1. Fabrication of PNC and HRPS

The fabrication process for the PNC is illustrated in **Figure 1**a. A solution of hydroxyl-functionalized CNTs and chloroform was sonicated before and after adding uncured Ecoflex for a uniform dispersion of the CNTs (Figure S1, Supporting Information). The solution was heated and stirred to evaporate the chloroform until the weight ratio of chloroform and Ecoflex reached 10–1. A 650 μm thick nickel foam was used as the template for the PNC (Figure 1b) and was dipped into and then withdrawn from the solution mixture. The solution-coated nickel foam was heated at 150 °C for 30 min to fully evaporate the chloroform and cure the CNT-doped Ecoflex nanocomposite. Afterward, the sample was immersed in hydrochloric acid (HCl) to fully etch away the nickel. The leftover PNC was rinsed with distilled water. The final PNC has an 86% porous open-cell structure with tubular ligaments as shown in Figure 1c. The PNC is biocompatible due to the proven biocompatibility of Ecoflex and CNT nanocomposites.[72,73] More details on the fabrication procedures and materials used are available in the Experimental Section.

To construct the HRPS, a piece of PNC was sandwiched by two flexible electrodes with an ultrathin insulating layer added between the PNC and one side of the electrodes as illustrated in Figure 1d. The electrode layers were gold/polyimide (Au/PI) films and the insulating layer was a poly(methyl methacrylate) (PMMA) film with a thickness of only 500 nm. The multilayer was packaged between two transparent and soft 3M Tegaderm medical dressings. Although the PNC was electrically conductive, the PMMA film acted as an insulating layer, thus making

© 2021 Wiley-VCH GmbH

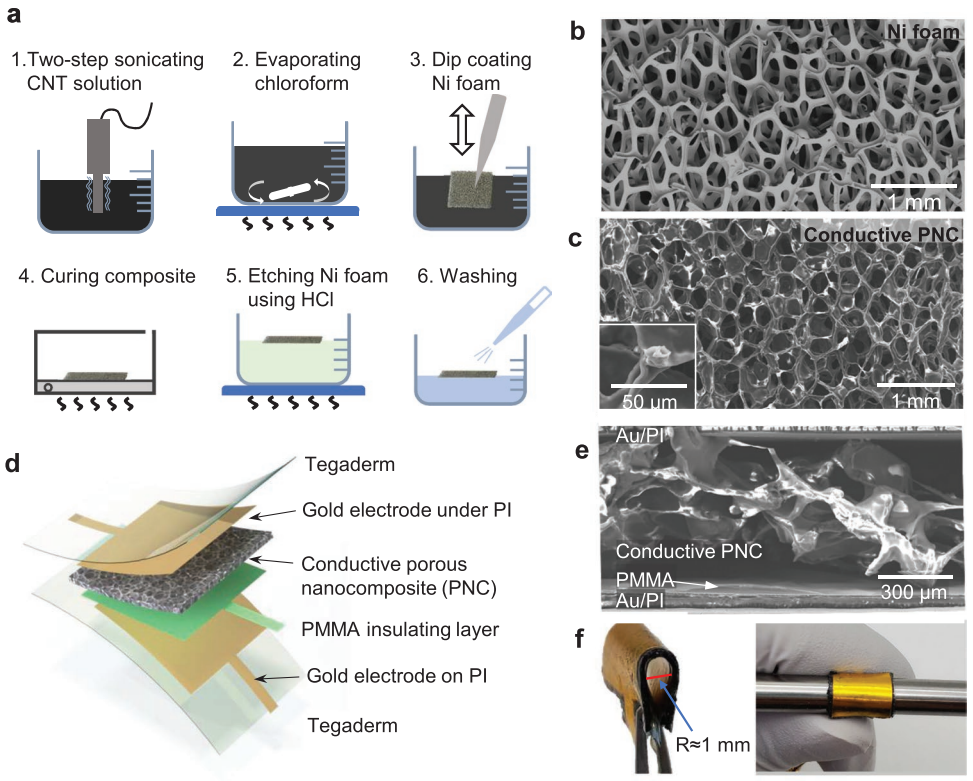

Figure 1. Fabrication of PNC and hybrid-response pressure sensor (HRPS). a) Schematic illustration of the fabrication process of the PNC. b) SEM image of an open cell nickel foam template for the fabrication of the PNC. c) SEM top-view of the PNC. A tubular ligament of PNC is included as an inset. d) Exploded schematic illustration of a HRPS. e) SEM cross-sectional view of the HRPS. f) Optical images of the HRPS (1×1 cm^2) bent by tweezers and on a cylindrical rod.

the whole pressure sensor capacitive. To prevent short circuits, the PMMA was transferred onto the Au/PI after the edges of the Au layer were slightly engraved by a laser cutter (Figure S2, Supporting Information). A cross-sectional scanning electron microscopy (SEM) image of the HRPS is shown in Figure 1e. The air gaps surrounding the conductive ligaments produced parasitic capacitances. The packaged HRPS was flexible enough to be bent to a radius of 1 mm as shown in Figure 1f; and Video S1 (Supporting Information). The estimated minimum bending radius is 271 μm as described in Figure S3 (Supporting Information).

2.2. Characterization of HRPS

The softness of the HRPS is best characterized by the nominal pressure–strain curve in **Figure 2**a. The highly porous structure leads to a strong nonlinear response. The HRPS is able to reach 50% compressive strain under just 2 kPa pressure, as evident in the blown-up chart. The low initial compressive modulus is associated with the collapse of the PNC cells due to the elastic bending and buckling of the microligaments.[74,75] The HRPS's high compliance is an important contributing factor to its high sensitivity. The electrical resistance versus compressive strain curves are plotted in a semilog chart in Figure 2b. The weight concentration of CNT in the nanocomposite varies from 0.25 to 1 wt%, and the resistance of the PNC is measured without the insulating layer (Figure S4, Supporting Information). The resistance initially decreases by orders of magnitude upon compression due to the increasing contact between conductive ligaments in the PNC, and later, from the densification of the CNT network in the nanocomposite.[75] As expected, the PNCs with greater CNT doping concentrations have lower initial and final resistance. The resistivities of the PNCs at 0.77 compressive strain are 53, 2.5 MΩ m, 100 and 7.1 kΩ m when CNT doping ratios are 0.25, 0.5, 0.75, and 1 wt%, respectively. The piezoresistivity (slopes of the curves in Figure 2b) varies depending on the CNT doping concentrations due to the nonlinear behaviors within the percolation zone (Figure S5, Supporting Information).[76,77]

The capacitance changes of HRPSs with varying amounts of CNT in the PNC are plotted in Figure 2c. In addition to the HRPS, a capacitive pressure sensor made out of undoped but porous Ecoflex was also included for comparison. Three samples were fabricated and tested for each CNT doping ratio (Figure S6, Supporting Information), and the intermediate pressure response curve from the samples was selected for plotting in Figure 2c. The relative standard deviation among the three samples does not exceed 11% within the plotted pressure range. It is obvious that a greater CNT wt% results in a larger absolute capacitance change of the HRPS upon compression. The monotonic dependence on CNT wt%, however, does not persist when the capacitance change is normalized by initial capacitance as shown in Figure 2d. Due to an abrupt increase

© 2021 Wiley-VCH GmbH

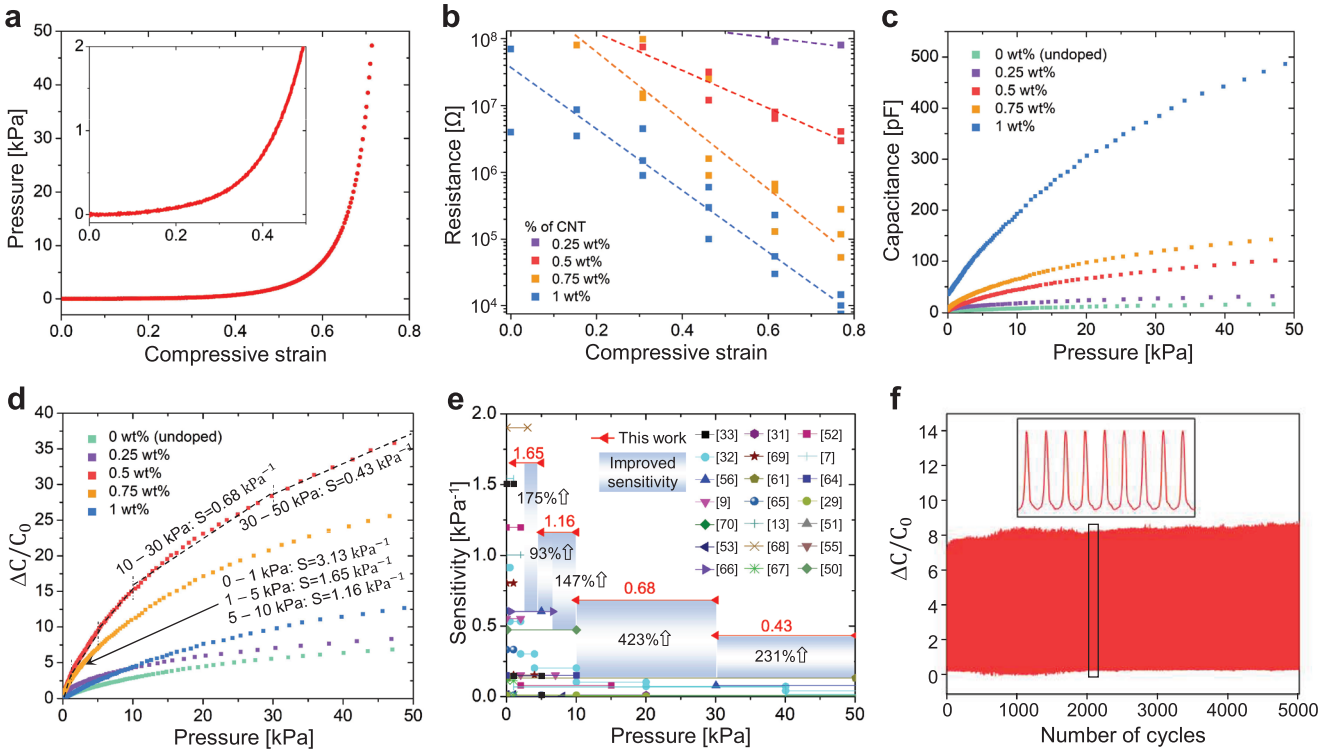

Figure 2. Electromechanical characterization of the HRPS. a) Pressure–strain curve of the HRPS. b) Resistance–strain curves of PNCs with different doping ratios of CNT. c) Pressure response of the absolute capacitance of the HRPS with different doping ratios of CNT. d) Pressure response of relative capacitance change of the HRPS with different doping ratios of CNT. 0.5 wt% appears to be the optimal doping concentration and tangential sensitivities are labeled for this curve. e) Comparison of the sensitivity of HRPS with capacitive pressure sensors reported in the literature in the pressure ranges of 1–5, 5–10, 10–30, and 30–50 kPa. f) Cyclic response of the HRPS up to 5000 cycles from 0 to 5 kPa.

in the initial capacitance when the CNT doping is beyond 0.5 wt% (Figure S7, Supporting Information), the HRPS with 0.5 wt% CNT PNC shows the highest sensitivity among the samples tested. Due to the existence of an optimal doping concentration, the HRPS is in distinct contrast to other capacitive pressure sensors, which always have higher sensitivities with larger amounts of conductive dopants which lead to higher dielectric constants.[60,67,68,71,78] The sensitivity of the HRPS changes with applied pressure and is found to be 3.13 kPa^{-1} within 0–1 kPa, 1.65 kPa^{-1} within 1–5 kPa, 1.16 kPa^{-1} within 5–10 kPa, 0.68 kPa^{-1} within 10–30 kPa, and 0.43 kPa^{-1} within 30–50 kPa when doped with 0.5 wt% CNT. The sensitivity of the HRPS exceeds that of other capacitive pressure sensors reported in the recent decade in the pressure range above 3 kPa (Figure 2e)[7,9,13,29–33,50–53,55,56,61,64–70]. Notably, this improvement is most impressive in the large pressure regime, with a maximum of 423% within 10–30 kPa. Such enhancement is explained through detailed comparisons of the HRPS with other types of capacitive pressure sensor and circuit models in the follows. The reversibility and durability of the HRPS are tested with 5000 repetitions of compression up to 5 kPa as shown in Figure 2f. The relative capacitance change increases by 12% after 1000 cycles and increases by an additional 3% after 5000 cycles. Loading-unloading and cyclic tests are also carried out with pressures reaching 50 kPa, and the results are offered in Figure S8 (Supporting Information). The hysteresis observed in Figure S8a (Supporting Information) is due to the instability of the micropores, which has been widely observed in other reported PNCs.[75,79,80] The slight drift of the baseline in Figure S8b (Supporting Information) is attributed to the irreversible pore structure changes induced by large pressure.[77]

2.3. Comparison of HRPS with other Conventional Capacitive Pressure Sensors

To demonstrate the superiority of the HRPS, four capacitive pressure sensors made with conventional dielectric materials (undoped solid Ecoflex, undoped porous Ecoflex, doped but nonconductive solid composite, and doped nonconductive PNC) were fabricated as shown in **Figure 3**a. All porous materials were fabricated using the same nickel foam template.

The 0.2 wt% CNT doping, which is just below the electrical percolation threshold, improves the dielectric constant of Ecoflex from 1.8 to 6.4 (Figure S9, Supporting Information). The four chosen dielectric layers well represent recent research advances in capacitive pressure sensors, which are adding air gaps (solid Ecoflex vs porous Ecoflex) and improving dielectric constant (solid Ecoflex vs nonconductive solid composite, porous Ecoflex vs nonconductive PNC). We compare the performance of these four conventional capacitive pressure sensors with our HRPS, which utilizes the conductive PNC with an insulating nanomembrane. 2D schematics of the conventional capacitive pressure sensors and HRPS are depicted in Figure 3b.

© 2021 Wiley-VCH GmbH

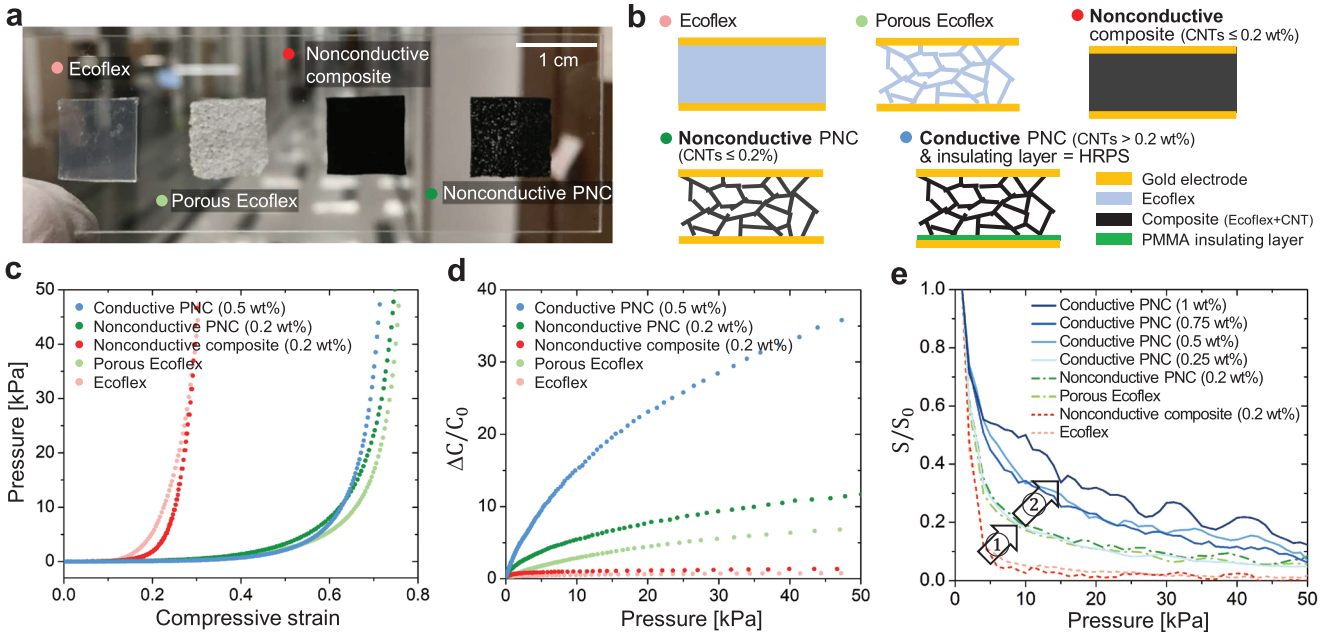

Figure 3. Comparison of HRPS and other capacitive pressure sensor counterparts. Red and pink represent solid layers, greens represent nonconductive porous layers, and blues represent conductive PNC. a) Photograph of four different dielectric materials with and without porosity and CNT-doping in Ecoflex. b) Schematic illustration of the four conventional capacitive pressure sensors and HRPS. c) Pressure–strain curves of all five capacitive pressure sensors. d) Relative capacitance changes of all five capacitive pressure sensors. e) Normalized tangential sensitivity vs pressure of all five capacitive pressure sensors. Arrow ① indicates enhancement due to porosity and Arrow ② due to the hybrid response of conductive PNC.

Figure 3c displays the pressure–strain curves of the five pressure sensors. Solids are clearly stiffer than porous materials, but the low CNT concentrations do not induce significant changes to the mechanical properties for either the solid or the porous materials.

The normalized capacitance versus pressure curves of the five different capacitive pressure sensors are shown in Figure 3d, and the sensitivities within the pressure ranges of 0–1, 1–5, 5–10, 10–30, and 30–50 kPa are plotted in Figure S10 (Supporting Information). As expected, adding air gaps improves the sensitivity of the capacitive pressure sensor (pink vs pale green curves in Figure 3d). Improving the dielectric constant of the ligaments in the porous dielectrics provide an additional significant enhancement to the sensitivity (pale green vs green curves in Figure 3d). However, increasing the dielectric constant of the solid dielectrics is not as effective in elevating sensitivity (pink vs red curves in Figure 3d). In fact, the dielectric constant of a solid should not affect sensitivity if it remains constant during compression. In reality, however, the dielectric constant does increase slightly with compression, as evident in Figure S9 (Supporting Information), due to the densification of the CNT network.[71] Among the four conventional capacitive pressure sensors, the one with nonconductive PNC (green curve) demonstrates the largest sensitivity due to the synergistic effects of air gaps and high dielectric constant ligaments. This sensitivity can be considered an upper limit for capacitive pressure sensors using dielectric materials because the porosity (86%) and the CNT loading (0.2 wt%) are both close to their thresholds. The sensitivity of the HRPS (blue curve) drastically surpasses all four conventional capacitive pressure sensors over all pressure ranges as evident in both Figure 3d; and Figure S10 (Supporting Information).

To investigate the decay in sensitivity with increased pressure, the tangential sensitivities of every kPa of all five capacitive pressure sensors are plotted against the applied pressure in Figure S11 (Supporting Information), and the normalized sensitivity (S/S_0) versus pressure is displayed in Figure 3e. Two major mechanisms for sensitivity enhancement, air gaps and the hybrid response, are indicated by the two arrows in the figure. First, when the dielectric material is solid (red and pink curves), with or without CNT doping, a sharp decrease of the normalized sensitivity occurs below 5 kPa. Therefore, these types of capacitive pressure sensors produce bilinear capacitance curves (Figure S12, Supporting Information), which are also widely observed with other early published capacitive pressure sensors.[9,33,71] The drastic drop of relative sensitivity is alleviated when the dielectric has a porous structure as demonstrated by Arrow ① in Figure 3e. This improvement is achieved through the enhanced effective compliance of the porous dielectric material caused by the bending and buckling of the ligaments.[74] Similar to the capacitive pressure sensor with solid dielectrics, the sensors with porous dielectrics exhibit the same tendency of relative sensitivity change with pressure independent of the CNT doping ratio, although their absolute sensitivities are very different. The second mechanism for the reduced declination of normalized sensitivity is attained through the hybrid response of the HRPS. For the HRPS with PNC doped with 0.25 wt% CNT (barely conductive), the normalized sensitivity curve is very similar to those of the capacitive pressure sensor made out of porous Ecoflex or nonconductive PNC. This is due to the piezocapacitive response still dominating the impedance of this barely conductive PNC. As the amount of CNT increases and the PNC resistance lowers,

© 2021 Wiley-VCH GmbH

the relative sensitivity trend is improved as demonstrated by Arrow ② in Figure 3e. In conclusion, these two mechanisms, air gaps, and hybrid responses, have distinctive effects in sustaining the sensitivity over a wide pressure range. On the other hand, increasing CNT doping can affect the absolute sensitivities but not necessarily the relative sensitivity.

3. Modeling the Hybrid Responses of HRPS

To offer a quantitative understanding of this new sensing mechanism, we model and compare the HRPS and a conventional pressure sensor using simplified equivalent circuits. The simplification process is described in Section 1A (Supporting Information), and a single inclined ligament with the open space as air is used to represent the PNC in **Figure 4**a–c. The equivalent circuit of a capacitive pressure sensor depends on the electrical property of the PNC. When the PNC ligaments are nonconductive and there is no added insulating layer, the electric field simply forms between the two parallel electrodes separated by a dielectric layer (Figure 4a). For the HRPS with a barely conductive PNC and an added insulating layer, there is a significant potential drop along the ligament, hence there is still a potential drop between the top electrode and the ligament (Figure 4b). For a HRPS with a more conductive PNC, the potential drop in the ligament becomes negligible such that there is no longer a potential drop between the top electrode and the ligament. In other words, the electric field only exists between the ligament and the bottom electrode, as illustrated in Figure 4c. In this case, since some of the air gaps are no longer within (and thus affecting) the electric field, the pressure sensitivity is expected to be compromised.

Based on these electric field models, equivalent circuits of capacitive pressure sensors with nonconductive PNC and high-resistivity conductive PNC were built such that the global capacitance change could be analyzed. The equivalent circuit for the capacitive pressure sensor with nonconductive PNC consists of some capacitance from the nonconductive composite ligaments ($C_{composite}$) in series with some capacitance from air gaps (C_{air}). These capacitances are in series because the electric field passes through one after another as depicted in Figure 4d. C_{air} and $C_{composite}$ are defined in the following expressions

$$C_{air} = \frac{k_{air}\varepsilon_0 A}{t(\varphi_0 - \epsilon)} \tag{1}$$

$$C_{composite} = \frac{k_{composite}\varepsilon_0 A}{t(1-\varphi_0)} \tag{2}$$

where k is the dielectric constant (k_{air} = 1), ε_0 is the permittivity of vacuum ($\varepsilon_0 = 8.85 \times 10^{-12}$ F m^{-1}), A is the area of the capacitive pressure sensor (e.g., $A = 1 \times 1$ cm^2), t is the initial thickness of the PNC (t = 650 µm), ϕ_0 is the initial porosity of the nanocomposite (ϕ_0 = 0.86), and ϵ is the nominal compressive strain. Assuming compression only affects the volume of air, only C_{air} is strain dependent. Using the equivalent circuit, global capacitance versus compressive strain for various $k_{composite}$ can be computed and is plotted in Figure 4e. As $k_{composite}$ increases from 2.5 (corresponding to $k_{Ecoflex}$) to 10 with increased CNT doping, the capacitance becomes more sensitive to strain, but the effect of k appears to saturate. The effect of $k_{composite}$ on the relative capacitance change is similar as shown in Figure 4f. This result verifies our previous observation that higher sensitivity is achieved with greater CNT doping in the nonconductive PNC.

The equivalent circuit for the HRPS with high-resistivity PNC is offered in Figure 4g. We model the piezocapacitive response due to the reduction of air gap as C_{air} and the piezoresistive response due to the contacts and collapses of tubular ligaments as $R_{composite}$. Since the nanocomposite is conductive, we no longer have $C_{composite}$. C_{air} and $R_{composite}$ are in parallel, and their combined impedance is in series to a fixed C_i representing the insulating PMMA nanomembrane. The capacitance of air and insulating layer can be expressed as

$$C_{air} = \frac{k_{air}\varepsilon_0 A}{t(\varphi_0 - \epsilon)} \tag{3}$$

$$C_i = \frac{k_{PMMA}\varepsilon_0 A}{t_{PMMA}} \tag{4}$$

where k_{air} = 1, k_{PMMA} = 4, and t_{PMMA} = 500 nm. The piezoresistive response of the conductive PNC can be fitted from our experimental measurements given in Figure 2b

$$R_{composite} = \frac{R_0}{\varphi_0^2}(\epsilon - \varphi_0)^2 + \frac{R_0}{1000} \tag{5}$$

where R_0 is the initial resistance of the conductive PNC before compression. Based on the circuit model, we calculate the capacitance versus strain response of the HRPS with various R_0, which is plotted in Figure 4h. The detailed derivations are provided in Section 1B (Supporting Information). The values of R_0 are hypothetical, but the range of R_0 is chosen to represent CNT concentrations from 0.25 wt% ($R_0 \approx 100$ GΩ) to 1 wt% ($R_0 \approx 10$ MΩ). As the initial resistance of the conductive PNC decreases, the initial capacitance of the HRPS increases. Notably, the initial capacitance of the sensor soars when R_0 is lower than 100 MΩ. The jump of initial capacitance would significantly reduce the relative capacitance change, thus explaining the nonmonotonic effect of R_0 in Figure 4i. Among the HRPSs with R_0 from 10 MΩ to 100 GΩ, the one with R_0 = 100 MΩ appears to have the highest sensitivity. This result agrees with our experimental finding that the optimal CNT loading with highest sensitivity is 0.5 wt% (Figure 2d). Comparing Figure 4i with Figure 4f, it is also obvious that the HRPS has a much higher sensitivity than the capacitive pressure sensor with nonconductive PNC.

Despite the fact that our theoretical results are obtained based on highly simplified equivalent circuit models, we are able to verify those results with experimental measurements. The analytical and experimental results for HRPSs with CNT doping ratios of 0.25, 0.5, 0.75, and 1 wt% are compared in Figure 4j–m. The strong agreement between the two in Figure 4j,k indicates that the equivalent circuit represents the hybrid sensing mechanism of the HRPS well. The analytical and experimental results start to deviate when the CNT doping ratio is 0.75 wt% (Figure 4l) and eventually become unrelated when the CNT doping ratio reaches 1 wt% (Figure 4m).

© 2021 Wiley-VCH GmbH

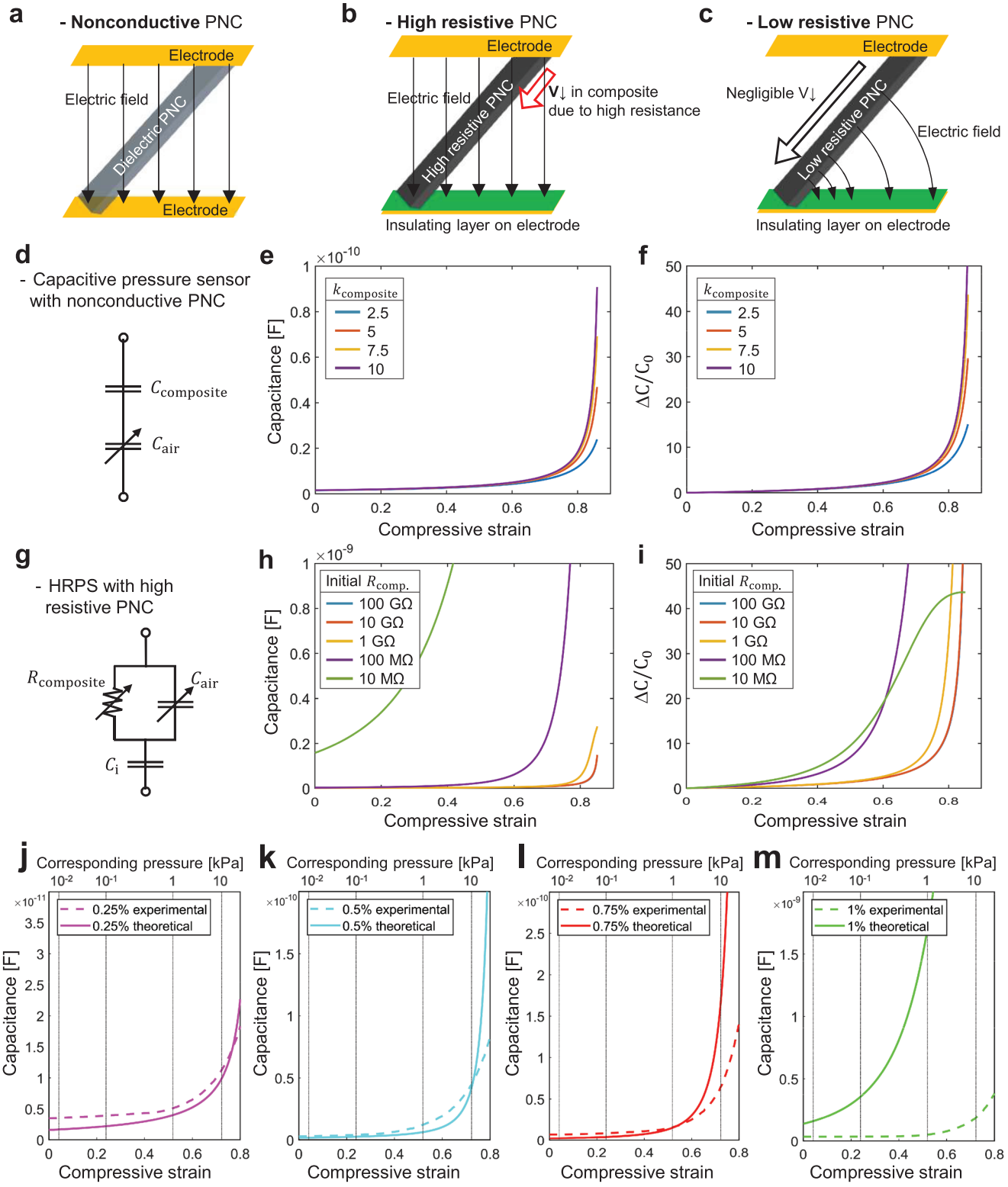

Figure 4. Analytical modeling of the HRPS and conventional capacitive pressure sensor with nonconductive PNC. a–c) Schematic illustrations of the electric fields of capacitive pressure sensors with nonconductive PNC (a), high-resistivity conductive PNC (b), and low-resistivity conductive PNC (c). d) Simplified equivalent circuit of capacitive pressure sensor with nonconductive PNC. e) Theoretical capacitance and f) relative capacitance changes for capacitive pressure sensor with nonconductive PNC of different dielectric constants. g) Simplified equivalent circuit of the HRPS with high-resistivity conductive PNC. h) Theoretical capacitance and i) relative capacitance of the HRPS with conductive PNC of different resistance. j–m) Theoretical (solid curves) and experimental (dashed curves) capacitance change of the HRPS with the CNT doping ratio of 0.25 wt% (j), 0.5 wt% (k), 0.75 wt% (l), and 1 wt% (m).

© 2021 Wiley-VCH GmbH

This could be explained by the schematic in Figure 4c—if the high conductivity of the nanocomposite ligaments completely changes the electric field, the equivalent circuit in Figure 4g is no longer applicable.

From both analytical calculation and experimental result, we conclude that there is an optimum resistance of conductive PNC. It should be low enough to warrant a large overall capacitance change of the HRPS but not so small that the initial capacitance becomes outrageous. As described in Section 1C (Supporting Information), the normalized capacitance change of HRPS can be analytically expressed according to the circuit model of Figure 4g. With the premise of $C_i >> C_{air}$ and taking a derivative with respect to R_0, we arrive to the following analytical expression of the optimal R_0

$$R_{0,\text{optimum}} = 7.7839\,\omega^{-1} C_{\text{air}_0}^{-\frac{3}{4}} C_i^{-\frac{1}{4}} \tag{6}$$

which indicates that the optimal R_0 is dictated by C_{air}, C_i, and the frequency at which the capacitance is measured (ω). Plugging in our experimental values of $\omega = 2\pi \cdot 1000$ rad s^{-1}, $C_{air0} = 1.58$ pF, and $C_i = 7.08$ nF, we estimated $R_{0,optimum} = 96$ MΩ, which agrees with our observation that $R_{0,optimum} = 100$ MΩ in Figure 4i. This optimized resistance is confirmed again in Figure S13 (Supporting Information), which displays R_0 with higher resolution than in Figure 4i. Consequently, as long as the geometry, porosity, insulating material, and measurement frequency of the HRPS are specified, the optimal resistance of the PNC can be easily identified using Equation (6). The detailed derivation is available in Section 1C (Supporting Information).

Although our theoretical analysis based on the highly simplified circuit model is able to offer a basic explanation for the hybrid effects and to predict the optimal CNT doping concentration, it still has room to improve. For example, the geometry of the pores was not considered in this model. Under the same porosity, the size and number of pores could vary greatly from sample to sample. In the case of very small pores and dense ligaments of the PNC, the $R_{composite}$ and C_{air} cannot be modeled as simply connected in parallel. Our model also omitted electrical contact resistance (ECR). With irregular contact between the PNC and the Au electrodes, the ECR is significant and cannot be neglected.[81] Although there is notable modeling work on electrically conductive solid nanocomposites, such as CNT doped in a silicone-based polymer,[82] there is no rigorous electromechanical models developed for conductive PNC so far. In order to fully understand the theoretical behavior of the HRPS, more accurate models that account for both ECR and conductive PNC need to be developed.

4. Demonstrations for HRPS

We designed several experiments to demonstrate the high sensitivity of the HRPS over a wide pressure range. Subtle pressures were applied on the HRPS in three different ways: without preload, with 1.5 kPa preload, and with 8 kPa preload.

First, tiny pressures that our skin experiences in daily life, such as the landing of a fly, a breeze, and water drops, were applied to the HRPS without preload. In **Figure 5**a, a 1×1 cm^2 HRPS detected the pressure applied by a 0.7 mg of drosophila, which corresponded to an effective average pressure of 0.07 Pa. In Figure 5b, the HRPS was able to sense breezes of air from an air blower 3 cm above the sensor. In Figure 5c, the HRPS could differentiate the pressures induced by three water droplets applied one after another. It demonstrated a response time of 94 ms, which was the time resolution of our LCR meter (Hioki 3532-50).

Second, we laminated a HRPS on human skin with preload to measure pulse waveforms. The carotid artery and the frontal temporal artery have well-known subtle pulsations[83] that require high sensitivity devices to detect. Figure 5d exhibits the location of the carotid artery and the temporal artery with benchmark arterial pulse waveforms obtained by medical gold standards, such as invasive arterial lines.[84–88] For the carotid arterial pulse (CAP), a HRPS was placed on the neck over the carotid artery packaged between two medical tapes (3M Tegaderm), which induced a preload of around 1.5 kPa over the HRPS as shown in Figure 5e. While the human subject held his breath, the CAP was clearly visible without any amplification or signal processing (Figure 5f). When the subject was breathing, respiration was visible as low-frequency undulations superimposed on the CAP as shown in Figure 5g. After applying a bandpass filter from 1 to 4 Hz, the CAP signal in Figure 5h appears similar to that in Figure 5f.

To induce a larger preload to the HRPS, the subject put on a virtual reality (VR) headset to cover a HRPS applied at the frontal temporal artery as shown in Figure 5i. The VR headset applied a preload of about 8 kPa over the HRPS. Even under a large preload, the unprocessed signal in Figure 5j demonstrates that heart rate measurements can be obtained from the temporal arterial pulse (TAP). After filtering the data using the same bandpass filter (1–4 Hz), a typical TAP waveform can be clearly observed in Figure 5k. To the best of our knowledge, this is the first capacitive pressure sensor able to detect the TAP. In addition to the CAP and TAP, the more widely measured radial arterial pulse (RAP) was also detectable by placing our packaged HRPS on the wrist as shown in Figure S14 (Supporting Information).

Finally, to demonstrate the HRPS's capabilities for detecting high pressure, we attached the HRPS to a 80 kg subject's planta and measured the pressure from footsteps on a soft yoga mat (Video S2, Supporting Information). The maximum footstep pressure recorded through the HRPS was 125 kPa and is comparable with other reported footstep pressures.[89]

5. Conclusions

Although ultrahigh sensitivity in soft capacitive pressure sensors has been achieved before, declining sensitivity with increasing pressure is a well-known and long-standing challenge. In this research, we introduced a novel flexible capacitive pressure sensor with high sensitivity over wide pressure ranges. By sandwiching an electrically conductive and highly porous nanocomposite and an ultrathin solid insulating layer between two parallel electrodes, our capacitive pressure sensor benefited from the combined piezoresistive and piezocapacitive responses of the PNC. Our HRPS achieved a sensitivity of

© 2021 Wiley-VCH GmbH

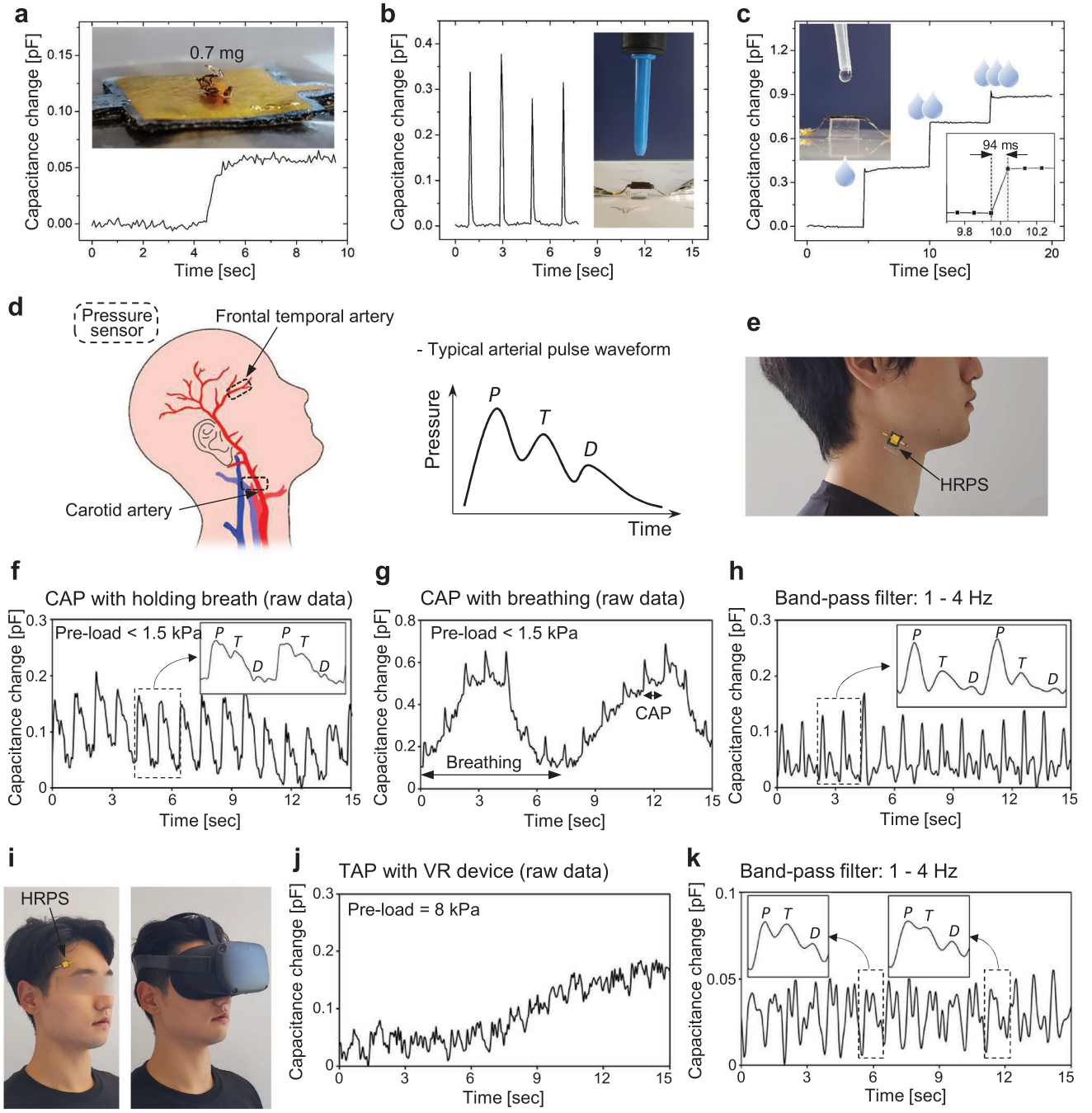

Figure 5. Demonstrations for HRPS. a) Detection of a 0.7 mg drosophila using a 1 × 1 cm^2 HRPS. The corresponding average effective pressure is 0.07 Pa. b) Detection of air flow coming out of an air blower 3 cm above the sensor. c) Detection of three successive waterdrops on the HRPS. d) Schematic illustration of carotid artery and temporal artery, and benchmarking waveforms of carotid arterial pulse (CAP) and temporal arterial pulse (TAP). e) Photograph of the HRPS installed on the skin over the carotid artery. A 3M Tegaderm tape was used for lamination, which induced a preload of 1.5 kPa. f) Capacitance response of CAP from a breath-holding subject. g) Capacitance response of CAP from a subject with normal breaths. h) Filtered CAP to eliminate respiratory signals from CAP. i) Photographs of a subject with an HRPS on the frontal temporal artery wearing a virtual reality (VR) headset over the HRPS. The VR headset applied 8 kPa preload on the HRPS. j) Unfiltered capacitance response of HRPS under the VR headset. k) Filtered TAP showing characteristic TAP peaks.

3.13 kPa^{-1} within 0–1 kPa, 1.65 kPa^{-1} within 1–5 kPa, 1.16 kPa^{-1} within 5–10 kPa, 0.68 kPa^{-1} within 10–30 kPa, and 0.43 kPa^{-1} within 30–50 kPa pressure ranges. By comparing the HRPS with four conventional capacitive pressure sensor counterparts, we successfully differentiated the contribution of air gaps from the hybrid responses. We established and experimentally validated a theoretical model which successfully unveils the sensing mechanism of the HRPS and analytically determines

© 2021 Wiley-VCH GmbH

the optimal PNC resistance controllable by tuning the CNT doping. We demonstrated the sensitivity of the HRPS by detecting subtle pressure changes with various preloads. Even when the HRPS was covered by a VR headset, we were able to obtain the first noninvasive measurement of the TAP with a skin mounted pressure sensor. The wide sensing range was manifested by plantar pressure sensing. In addition to pulse waveform sensing, our soft HRPS is also promising for many other potential uses in prosthesis, tactile sensing, and e-skin for surgical or soft robots.

Because of the hybrid responses of HRPS, opportunities for further improvement lie in the tuning of the piezoresistivity and piezocapacitive of the PNC through material and structure engineering. For instance, combining two or more types of conductive fillers in the porous composite can result in larger variations of resistance in response to pressure.[90] Applied to the HRPS, the enhanced piezoresistivity may result in a higher sensitivity of the sensors. Other types of porous structures could also benefit the HRPS. For example, a hierarchical porous structure can generate high piezoresistivity over a wide pressure range by facilitating a balanced load transfer through the structure.[91] Such structures may enhance both the sensitivity and the cycleability of the HRPS over wide pressure ranges.

6. Experimental Section

PNC Fabrication: A mixture of hydroxyl functionalized multiwall carbon nanotubes (Carbon Nanotubes Plus) and chloroform (Sigma-Aldrich) was prepared with a ratio of 1 mg CNT: 2 chloroform. For 0.25 wt% CNT-doped PNC, the ratio was 1:3 considering the dilution ratio of Ecoflex in the chloroform. The solution was sonicated by a sonicator (Q500, QSonica) with a power of 500 watts for 10 min. Uncured Ecoflex (Ecoflex 00–30, Smooth-on) base polymer was then added to the solution according to the target doping ratio of CNT, and the new mixture was sonicated for 10 min. After sonication, the solution was heated and stirred at 100 °C and 400 rpm using a magnetic hotplate stirrer (Fisher Scientific) to evaporate the chloroform. When the chloroform to Ecoflex weight ratio reached 10:1, a nickel foam (Tmax) was dipped into the solution for 5 s and then extracted and put in a 150 °C oven for 30 min to fully evaporate the chloroform and cure the CNT-Ecoflex composite. The whole specimen was immersed in a 3 M HCl (hydrochloric acid, Sigma-Aldrich) at 80 °C for 12 h to etch the nickel foam template. Finally, the PNC was washed with distilled water.

Dielectric Materials Fabrication: Nonporous Ecoflex: Ecoflex was molded in a 1 cm × 1 cm × 650 µm CNC-machined poly(tetrafluoroethylene) (PTFE) (McMaster-Carr) mold and cured in the oven at 150 °C for 30 min. Porous Ecoflex: a nickel foam was dipped into a 10:1 diluted Ecoflex by chloroform for 5 s. After that, the process followed that of PNC. Nonporous nanocomposite: the solution of CNT and chloroform was sonicated twice before and after adding Ecoflex for 10 min, and the chloroform was fully evaporated with stirring at 600 rpm. The leftover composite of CNT and Ecoflex was molded in the PTFE mold and cured in an oven at 150 °C for 30 min.

Fabrication of 500 nm Thick Insulating Layer: Poly(vinyl alcohol) (PVA) solution, Flinn Scientific) was spin-coated on the silicon wafer at 1000 rpm for 45 s and baked at 70 °C for 1 min as a releasing agent. PMMA (PMMA A4, MicroChem) was spin-coated on the PVA at 300 rpm for 45 s and baked at 180 °C for 2 min. When immersed in a deionized water bath, the PVA layer was dissolved and the PMMA film floated to the surface of water. A temporary tattoo paper (Silhouette temporary tattoo paper, Silhouette) was used to pick up the PMMA film and the PMMA/tattoo paper was dried on a hot plate at 50 °C for 30 min. The PMMA could be transferred to other surfaces by smearing water to the tattoo paper.

HRPS Fabrication: A 100 nm gold-on-13 µm polyimide (PI) bilayer (Sheldahl) was tailored into the desired electrode design. The gold layer was engraved by a width of 100 µm from all edges through laser beam machining (ProtoLaser U4, LPKF). The Au/PI electrode was attached to a 3M Tegaderm tape and the insulating PMMA layer was transferred onto the electrode. Finally, the conductive PNC was sandwiched between a Au/PI/Tegaderm film and a PMMA/Au/PI/Tegaderm film.

Compression Testing: A Dynamic Mechanical Analyzer (RSA-G2, TA Instruments) was used to control and measure the applied pressure and displacement. The resistance of the conductive PNC was measured by a digital multimeter (DM3068, Rigol), and the impedance of the HRPS was measured by an LCR meter (3532-50, Hioki) at 1 kHz frequency with a 2 V AC signal, both in situ.

Calculation of PNC Porosity: After measurement of the weight and volume of the PNC, porosity was calculated based on the density of Ecoflex and CNT.

Definition of Electrical Percolation Threshold: The traditional definition of electrical percolation threshold is the point at which the direct current (DC) conductivity rises the most rapidly with increases in filler concentrations. In the research, the material's electrical impedance under alternating current (AC) was measured to obtain both capacitance and resistance. The electrical percolation threshold was defined by the phase of the impedance. A nanocomposite containing resistive and reactive components has a phase angle between 0° (purely resistive) and −90° (purely capacitive). The porous composite was determined to be conductive if its phase angle was measured to be between 0° and −3° during compression up to 50 kPa.

Calculation of Sensitivity of Pressure Sensors Every kPa: After calculating the normalized capacitance of pressure sensors, they were 1D interpolated by pressure to get enough data points for an accurate sensitivity determination. Then, the sensitivity in every kPa was calculated using linear regression and smoothing via moving average filter.

Measurement of Arterial Pulses: The arterial pulses were measured while the subject lied supine on a bed. For the detection of carotid arterial pulses, the subject rotated their neck by 45°.

Experiments on Human Subjects: All measurement on human subjects were conducted under approval from the Institutional Review Board of the University of Texas at Austin (protocol no.: 2015-05-0024). Informed consent was obtained from all subjects involved in the study.

Supporting Information

Supporting Information is available from the Wiley Online Library or from the author.

Acknowledgements

This research was sponsored partially by the US Office of Naval Research under the Grant No. N00014-20-1-2112 and partially by the US Army Research Office under Cooperative Agreement No. W911NF-19-2-0333. The research facility is partially supported by the US Office of Naval Research under Grant No. N00014-18-1-2323. The views and conclusions contained in this document are those of the authors and should not be interpreted as representing the official policies, either expressed or implied, of the Office of Naval Research, the Army Research Office, or the U.S. Government. The U.S. Government is authorized to reproduce and distribute reprints for Government purposes notwithstanding any copyright notation herein. N.L. acknowledges the Temple Foundation Endowed Teaching Fellowship in Engineering No. 1. K.-H.H. acknowledges the Philip C. and Linda L. Lewis Foundation Graduate Fellowship in Mechanical Engineering and the Warren A. and Alice L. Meyer Endowed Scholarship in Engineering at the University of Texas at Austin. Ethical approval was not required for the experiments with drosophila. The image of one of the authors appears in Figure 5e,i with their consent for publication here and for future reproductions such as in review articles.

© 2021 Wiley-VCH GmbH

Conflict of Interest

The authors declare no conflict of interest.

Data Availability Statement

The data that support the findings of this study are available from the corresponding author upon reasonable request.

Keywords

conductive foams, e-skins, flexible electronics, porous nanocomposites, pressure sensors, pulse waveforms

Received: April 30, 2021
Revised: July 27, 2021
Published online:

[1] S.-H. Sunwoo, K.-H. Ha, S. Lee, N. Lu, D.-H. Kim, *Annu. Rev. Chem. Biomol. Eng.* **2021**, *12*, 359.
[2] S. Xiang, D. Liu, C. Jiang, W. Zhou, D. Ling, W. Zheng, X. Sun, X. Li, Y. Mao, C. Shan, *Adv. Funct. Mater.* **2021**, *31*, 2100940.
[3] Y. Tang, H. Zhou, X. Sun, N. Diao, J. Wang, B. Zhang, C. Qin, E. Liang, Y. Mao, *Adv. Funct. Mater.* **2020**, *30*, 1907893.
[4] C. M. Boutry, M. Negre, M. Jorda, O. Vardoulis, A. Chortos, O. Khatib, Z. Bao, *Sci. Robot.* **2018**, *3*, eaau6914.
[5] W. W. Lee, Y. J. Tan, H. Yao, S. Li, H. H. See, M. Hon, K. A. Ng, B. Xiong, J. S. Ho, B. C. Tee, *Sci. Robot.* **2019**, *4*, eaax2198.
[6] M. Liu, X. Pu, C. Jiang, T. Liu, X. Huang, L. Chen, C. Du, J. Sun, W. Hu, Z. L. Wang, *Adv. Mater.* **2017**, *29*, 1703700.
[7] Y. Wan, Z. Qiu, J. Huang, J. Yang, Q. Wang, P. Lu, J. Yang, J. Zhang, S. Huang, Z. Wu, C. F. Guo, *Small* **2018**, *14*, e1801657.
[8] H.-H. Chou, A. Nguyen, A. Chortos, J. W. To, C. Lu, J. Mei, T. Kurosawa, W.-G. Bae, J. B.-H. Tok, Z. Bao, *Nat. Commun.* **2015**, *6*, 8011.
[9] S. C. Mannsfeld, B. C. Tee, R. M. Stoltenberg, C. V. H. Chen, S. Barman, B. V. Muir, A. N. Sokolov, C. Reese, Z. Bao, *Nat. Mater.* **2010**, *9*, 859.
[10] Y. Gao, H. Ota, E. W. Schaler, K. Chen, A. Zhao, W. Gao, H. M. Fahad, Y. Leng, A. Zheng, F. Xiong, *Adv. Mater.* **2017**, *29*, 1701985.
[11] K. Meng, J. Chen, X. Li, Y. Wu, W. Fan, Z. Zhou, Q. He, X. Wang, X. Fan, Y. Zhang, *Adv. Funct. Mater.* **2019**, *29*, 1806388.
[12] S. Lee, A. Reuveny, J. Reeder, S. Lee, H. Jin, Q. Liu, T. Yokota, T. Sekitani, T. Isoyama, Y. Abe, *Nat. Nanotechnol.* **2016**, *11*, 472.
[13] H. Kim, G. Kim, T. Kim, S. Lee, D. Kang, M. S. Hwang, Y. Chae, S. Kang, H. Lee, H. G. Park, *Small* **2018**, *14*, 1703432.
[14] M. Kaltenbrunner, T. Sekitani, J. Reeder, T. Yokota, K. Kuribara, T. Tokuhara, M. Drack, R. Schwödiauer, I. Graz, S. Bauer-Gogonea, *Nature* **2013**, *499*, 458.
[15] C. L. Choong, M. B. Shim, B. S. Lee, S. Jeon, D. S. Ko, T. H. Kang, J. Bae, S. H. Lee, K. E. Byun, J. Im, *Adv. Mater.* **2014**, *26*, 3451.
[16] C. Pang, G.-Y. Lee, T.-i. Kim, S. M. Kim, H. N. Kim, S.-H. Ahn, K.-Y. Suh, *Nat. Mater.* **2012**, *11*, 795.
[17] C. M. Boutry, A. Nguyen, Q. O. Lawal, A. Chortos, S. Rondeau-Gagné, Z. Bao, *Adv. Mater.* **2015**, *27*, 6954.
[18] J. H. Kim, J. Caprioli, *J. Ophthalmic Vis. Res.* **2018**, *13*, 170.
[19] C. Robba, D. Cardim, T. Tajsic, J. Pietersen, M. Bulman, J. Donnelly, A. Lavinio, A. Gupta, D. K. Menon, P. J. Hutchinson, *PLoS Med.* **2017**, *14*, e1002356.
[20] Y. Zang, F. Zhang, C.-a. Di, D. Zhu, *Mater. Horiz.* **2015**, *2*, 140.
[21] Z. Li, Z. L. Wang, *Adv. Mater.* **2011**, *23*, 84.
[22] C. Lou, S. Wang, T. Liang, C. Pang, L. Huang, M. Run, X. Liu, *Materials* **2017**, *10*, 1068.
[23] K. He, Y. Hou, C. Yi, N. Li, F. Sui, B. Yang, G. Gu, W. Li, Z. Wang, Y. Li, *Nano Energy* **2020**, *73*, 104743.
[24] L. Zhao, F. Qiang, S. Dai, S. Shen, Y. Huang, N.-J. Huang, G. Zhang, L.-Z. Guan, J. Gao, Y. Song, L.-C. Tang, *Nanoscale* **2019**, *11*, 10229.
[25] Y. Lee, J. Park, S. Cho, Y.-E. Shin, H. Lee, J. Kim, J. Myoung, S. Cho, S. Kang, C. Baig, *ACS Nano* **2018**, *12*, 4045.
[26] M. T. Chorsi, E. J. Curry, H. T. Chorsi, R. Das, J. Baroody, P. K. Purohit, H. Ilies, T. D. Nguyen, *Adv. Mater.* **2019**, *31*, 1802084.
[27] J. Chun, K. Y. Lee, C. Y. Kang, M. W. Kim, S. W. Kim, J. M. Baik, *Adv. Funct. Mater.* **2014**, *24*, 2038.
[28] W. Choi, J. Lee, Y. Kyoung Yoo, S. Kang, J. Kim, J. Hoon Lee, *Appl. Phys. Lett.* **2014**, *104*, 123701.
[29] H. Shi, M. Al-Rubaiai, C. M. Holbrook, J. Miao, T. Pinto, C. Wang, X. Tan, *Adv. Funct. Mater.* **2019**, *29*, 1809116.
[30] S. R. A. Ruth, L. Beker, H. Tran, V. R. Feig, N. Matsuhisa, Z. Bao, *Adv. Funct. Mater.* **2019**, *30*, 1903100.
[31] C. G. Núñez, W. T. Navaraj, E. O. Polat, R. Dahiya, *Adv. Funct. Mater.* **2017**, *27*, 1606287.
[32] L. Viry, A. Levi, M. Totaro, A. Mondini, V. Mattoli, B. Mazzolai, L. Beccai, *Adv. Mater.* **2014**, *26*, 2659.
[33] S. Park, H. Kim, M. Vosgueritchian, S. Cheon, H. Kim, J. H. Koo, T. R. Kim, S. Lee, G. Schwartz, H. Chang, *Adv. Mater.* **2014**, *26*, 7324.
[34] C. Hou, Z. Xu, W. Qiu, R. Wu, Y. Wang, Q. Xu, X. Y. Liu, W. Guo, *Small* **2019**, *15*, 1805084.
[35] M. Ramuz, B. C. K. Tee, J. B. H. Tok, Z. Bao, *Adv. Mater.* **2012**, *24*, 3223.
[36] Y. Yamada, T. Morizono, Y. Umetani, H. Takahashi, *IEEE Trans. Ind. Electron.* **2005**, *52*, 960.
[37] V. Amoli, J. S. Kim, S. Y. Kim, J. Koo, Y. S. Chung, H. Choi, D. H. Kim, *Adv. Funct. Mater.* **2019**, *30*, 1904532.
[38] Y. Chang, L. Wang, R. Li, Z. Zhang, Q. Wang, J. Yang, C. F. Guo, T. Pan, *Adv. Mater.* **2021**, *33*, 2003464.
[39] S. K. Ravi, N. Paul, L. Suresh, A. T. Salim, T. Wu, Z. Wu, M. R. Jones, S. C. Tan, *Mater. Horiz.* **2020**, *7*, 866.
[40] A. Chortos, J. Liu, Z. Bao, *Nat. Mater.* **2016**, *15*, 937.
[41] M. L. Hammock, A. Chortos, B. C. K. Tee, J. B. H. Tok, Z. Bao, *Adv. Mater.* **2013**, *25*, 5997.
[42] J. Li, R. Bao, J. Tao, Y. Peng, C. Pan, *J. Mater. Chem. C* **2018**, *6*, 11878.
[43] H. Yousef, M. Boukallel, K. Althoefer, *Sens. Actuators A* **2011**, *167*, 171.
[44] N. Bai, L. Wang, Q. Wang, J. Deng, Y. Wang, P. Lu, J. Huang, G. Li, Y. Zhang, J. Yang, *Nat. Commun.* **2020**, *11*, 209.
[45] Q. Liu, Z. Liu, C. Li, K. Xie, P. Zhu, B. Shao, J. Zhang, J. Yang, J. Zhang, Q. Wang, *Adv. Sci.* **2020**, *7*, 2000348.
[46] S. H. Cho, S. W. Lee, S. Yu, H. Kim, S. Chang, D. Kang, I. Hwang, H. S. Kang, B. Jeong, E. H. Kim, S. M. Cho, K. L. Kim, H. Lee, W. Shim, C. Park, *ACS Appl. Mater. Interfaces* **2017**, *9*, 10128.
[47] B. Nie, R. Li, J. Cao, J. D. Brandt, T. Pan, *Adv. Mater.* **2015**, *27*, 6055.
[48] Z. Zhu, R. Li, T. Pan, *Adv. Mater.* **2018**, *30*, 1705122.
[49] S. Qiao, N. Lu, *Int. J. Solids Struct.* **2015**, *58*, 353.
[50] Y. Xiong, Y. Shen, L. Tian, Y. Hu, P. Zhu, R. Sun, C.-P. Wong, *Nano Energy* **2020**, *70*, 104436.
[51] J. Yang, S. Luo, X. Zhou, J. Li, J. Fu, W. Yang, D. Wei, *ACS Appl. Mater. Interfaces* **2019**, *11*, 14997.
[52] Y. Wan, Z. Qiu, Y. Hong, Y. Wang, J. Zhang, Q. Liu, Z. Wu, C. F. Guo, *Adv. Electron. Mater.* **2018**, *4*, 1700586.
[53] S. Baek, H. Jang, S. Y. Kim, H. Jeong, S. Han, Y. Jang, D. H. Kim, H. S. Lee, *RSC Adv.* **2017**, *7*, 39420.
[54] Q. Zhou, B. Ji, Y. Wei, B. Hu, Y. Gao, Q. Xu, J. Zhou, B. Zhou, *J. Mater. Chem. A* **2019**, *7*, 27334.

© 2021 Wiley-VCH GmbH

[55] J. C. Yang, J.-O. Kim, J. Oh, S. Y. Kwon, J. Y. Sim, D. W. Kim, H. B. Choi, S. Park, *ACS Appl. Mater. Interfaces* **2019**, *11*, 19472.
[56] D. Kwon, T.-I. Lee, M. Kim, S. Kim, T.-S. Kim, I. Park in *2015 Transducers - 2015 18th Int. Conf. on Solid-State Sensors, Actuators and Microsystems (TRANSDUCERS)*, IEEE, Piscataway, NJ, USA **2015**, pp. 299–302, https://doi.org/10.1109/TRANSDUCERS.2015.7180920.
[57] J. Hwang, Y. Kim, H. Yang, J. H. Oh, *Composites, Part B* **2021**, *211*, 108607.
[58] A. Chhetry, S. Sharma, H. Yoon, S. Ko, J. Y. Park, *Adv. Funct. Mater.* **2020**, *30*, 1910020.
[59] R. Y. Tay, H. Li, J. Lin, H. Wang, J. S. K. Lim, S. Chen, W. L. Leong, S. H. Tsang, E. H. T. Teo, *Adv. Funct. Mater.* **2020**, *30*, 1909604.
[60] J. Yang, D. Tang, J. Ao, T. Ghosh, T. V. Neumann, D. Zhang, E. Piskarev, T. Yu, V. K. Truong, K. Xie, *Adv. Funct. Mater.* **2020**, *30*, 2002611.
[61] W. Cheng, L. Yu, D. Kong, Z. Yu, H. Wang, Z. Ma, Y. Wang, J. Wang, L. Pan, Y. Shi, *IEEE Electron Device Lett.* **2018**, *39*, 1069.
[62] S. Lee, S. Franklin, F. A. Hassani, T. Yokota, M. O. G. Nayeem, Y. Wang, R. Leib, G. Cheng, D. W. Franklin, T. Someya, *Science* **2020**, *370*, 966.
[63] C. C. Vu, J. Kim, *Sens. Actuators A* **2020**, *314*, 112029.
[64] J. Kim, E. F. Chou, J. Le, S. Wong, M. Chu, M. Khine, *Adv. Healthcare Mater.* **2019**, *8*, 1900109.
[65] Z. He, W. Chen, B. Liang, C. Liu, L. Yang, D. Lu, Z. Mo, H. Zhu, Z. Tang, X. Gui, *ACS Appl. Mater. Interfaces* **2018**, *10*, 12816.
[66] Y. Joo, J. Yoon, J. Ha, T. Kim, S. Lee, B. Lee, C. Pang, Y. Hong, *Adv. Electron. Mater.* **2017**, *3*, 1600455.
[67] S.-Y. Liu, J.-G. Lu, H.-P. D. Shieh, *IEEE Sens. J.* **2018**, *18*, 1870.
[68] F. Liu, F. Han, L. Ling, J. Li, S. Zhao, T. Zhao, X. Liang, D. Zhu, G. Zhang, R. Sun, D. Ho, C. P. Wong, *Chem. – Eur. J.* **2018**, *24*, 16823.
[69] S. Wan, H. Bi, Y. Zhou, X. Xie, S. Su, K. Yin, L. Sun, *Carbon* **2017**, *114*, 209.
[70] X. Guo, Y. Huang, X. Cai, C. Liu, P. Liu, *Meas. Sci. Technol.* **2016**, *27*, 045105.
[71] J. Wang, J. Jiu, M. Nogi, T. Sugahara, S. Nagao, H. Koga, P. He, K. Suganuma, *Nanoscale* **2015**, *7*, 2926.
[72] J. H. Kim, J.-Y. Hwang, H. R. Hwang, H. S. Kim, J. H. Lee, J.-W. Seo, U. S. Shin, S.-H. Lee, *Sci. Rep.* **2018**, *8*, 1375.
[73] W. J. Bae, J. B. Choi, K. S. Kim, S. J. Kim, H. J. Cho, U. S. Ha, S. H. Hong, J. Y. Lee, S. W. Kim, *Transl. Androl. Urol.* **2015**, AB168.
[74] D. V. W. M. De Vries, *Characterization of Polymeric Foams*, Eindhoven University of Technology, Eindhoven, The Netherlands **2009**; available at https://www.mate.tue.nl/mate/pdfs/10702_sec.pdf
[75] L. Gong, S. Kyriakides, W.-Y. Jang, *Int. J. Solids Struct.* **2005**, *42*, 1355.
[76] T. Zhai, D. Li, G. Fei, H. Xia, *Composites, Part A* **2015**, *72*, 108.
[77] M. Panahi-Sarmad, M. Noroozi, M. Abrisham, S. Eghbalinia, F. Teimoury, A. R. Bahramian, P. Dehghan, M. Sadri, V. Goodarzi, *ACS Appl. Electron. Mater.* **2020**, *2*, 2318.
[78] M. Pruvost, W. J. Smit, C. Monteux, P. Poulin, A. Colin, *npj Flex. Electron.* **2019**, *3*, 7.
[79] Y. Si, L. Wang, X. Wang, N. Tang, J. Yu, B. Ding, *Adv. Mater.* **2017**, *29*, 1700339.
[80] R. Widdle Jr., A. Bajaj, P. Davies, *Int. J. Eng. Sci.* **2008**, *46*, 31.
[81] N. Khalili, H. Naguib, R. Kwon, *Soft Matter* **2016**, *12*, 4180.
[82] L. Jin, A. Chortos, F. Lian, E. Pop, C. Linder, Z. Bao, W. Cai, *Proc. Natl. Acad. Sci. USA* **2018**, *115*, 1986.
[83] R. E. Curran, *Arch. Ophthalmol.* **1986**, *104*, 1756.
[84] G. Chen, C. Au, J. Chen, *Trends Biotechnol.* **2021**.
[85] B. Campbell, *Heart Lung* **1997**, *26*, 204.
[86] H. K. Walker, W. D. Hall, J. W. Hurst, *Clinical Methods: The History, Physical, and Laboratory Examinations*, Butterworth-Heinemann, Boston, MA, USA **1990**.
[87] A. Cournand, H. A. Ranges, *Proc. Soc. Exp. Biol. Med.* **1941**, *46*, 462.
[88] M.-M. Laurila, M. Peltokangas, K. L. Montero, T. Siponkoski, J. Juuti, S. Tuukkanen, N. Oksala, A. Vehkaoja, M. Mäntysalo, *IEEE Sens. J.* **2019**, *19*, 11072.
[89] J. Tao, M. Dong, L. Li, C. Wang, J. Li, Y. Liu, R. Bao, C. Pan, *Microsyst. Nanoeng.* **2020**, *6*, 62.
[90] Z. Ma, A. Wei, J. Ma, L. Shao, H. Jiang, D. Dong, Z. Ji, Q. Wang, S. Kang, *Nanoscale* **2018**, *10*, 7116.
[91] L. Yang, Y. Liu, C. D. Filipe, D. Ljubic, Y. Luo, H. Zhu, J. Yan, S. Zhu, *ACS Appl. Mater. Interfaces* **2019**, *11*, 4318.

© 2021 Wiley-VCH GmbH

© 2021 Wiley-VCH GmbH

ADVANCED MATERIALS

Supporting Information

for *Adv. Mater.,* DOI: 10.1002/adma.202103320

Highly Sensitive Capacitive Pressure Sensors over a Wide Pressure Range Enabled by the Hybrid Responses of a Highly Porous Nanocomposite

*Kyoung-Ho Ha, Weiyi Zhang, Hongwoo Jang, Seungmin Kang, Liu Wang, Philip Tan, Hochul Hwang, and Nanshu Lu**

Supporting Information

Highly sensitive capacitive pressure sensors over a wide pressure range enabled by the hybrid responses of a highly porous nanocomposite

*Kyoung-Ho Ha, Weiyi Zhang, Hongwoo Jang, Seungmin Kang, Liu Wang, Philip Tan, Hochul Hwang, Nanshu Lu**

Section 1. Analytical calculation

A. Simplification of equivalent circuits of capacitive pressure sensors

- Capacitive pressure sensor with a nonconductive PNC

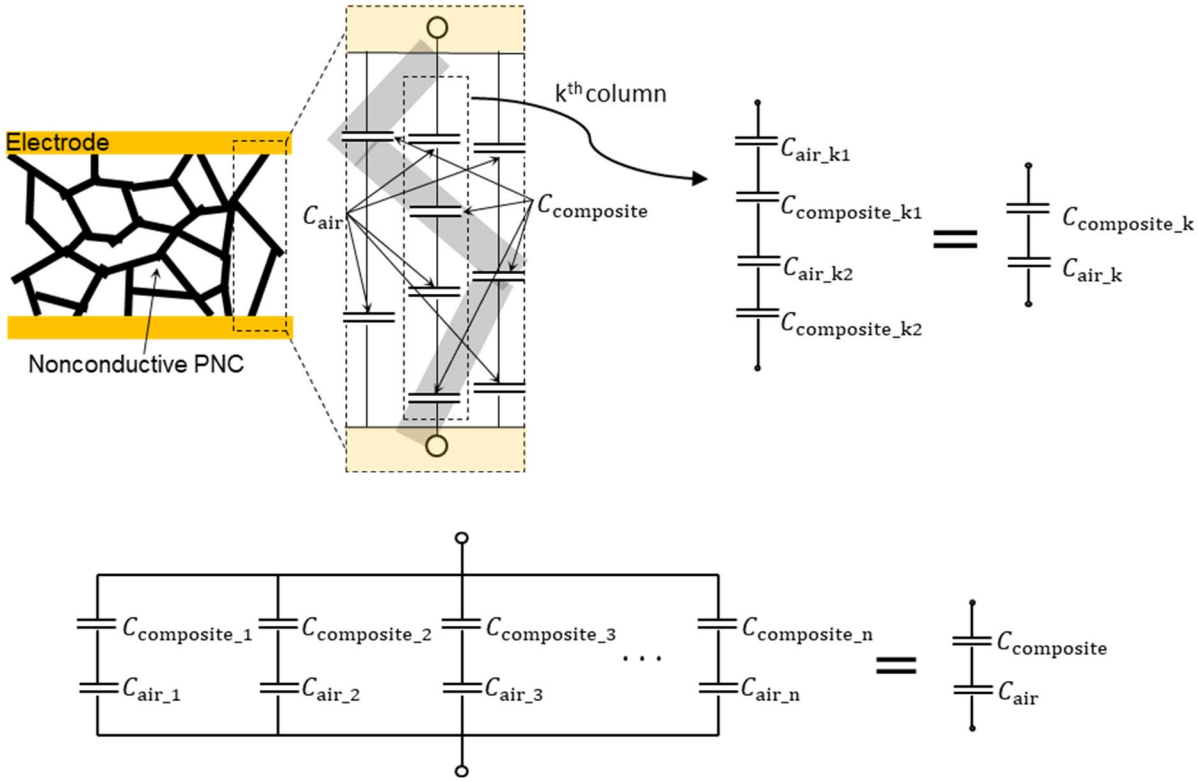

Figure SA1. Simplification of the equivalent circuit of a capacitive pressure sensor with a nonconductive porous nanocomposite (PNC)

The area of the sensor (A) is first divided by n. Therefore, the equivalent circuit of the capacitive pressure sensor can be described by n columns in parallel.

$$A_{\mathrm{n}} = \frac{1}{n}A \qquad (1)$$

In the k[th] column of the equivalent circuit, all impedance (Z) of C_{air} and $C_{\mathrm{composite}}$ which are connected in series can merge, as described below.

$$Z_{\mathrm{k}} = Z_{\mathrm{air\_k1}} + Z_{\mathrm{composite\_k1}} + Z_{\mathrm{air\_k2}} + Z_{\mathrm{composite\_k2}}$$

$$= \frac{1}{j\omega C_{\mathrm{air\_k1}}} + \frac{1}{j\omega C_{\mathrm{composite\_k1}}} + \frac{1}{j\omega C_{\mathrm{air\_k2}}} + \frac{1}{j\omega C_{\mathrm{composite\_k2}}}$$

$$= \frac{t_{\mathrm{air\_k1}}}{j\omega A_n k_{\mathrm{air}}\varepsilon_0} + \frac{t_{\mathrm{composite\_k1}}}{j\omega A_n k_{\mathrm{composite}}\varepsilon_0} + \frac{t_{\mathrm{air\_k2}}}{j\omega A_n k_{\mathrm{air}}\varepsilon_0} + \frac{t_{\mathrm{composite\_k2}}}{j\omega A_n k_{\mathrm{composite}}\varepsilon_0}$$

$$= \frac{t_{\mathrm{air\_k1}}+t_{\mathrm{air\_k2}}}{j\omega A_n k_{\mathrm{air}}\varepsilon_0} + \frac{t_{\mathrm{composite\_k1}}+t_{\mathrm{composite\_k2}}}{j\omega A_n k_{\mathrm{composite}}\varepsilon_0}$$

$$= \frac{t_{\mathrm{air\_k}}}{j\omega A_n k_{\mathrm{air}}\varepsilon_0} + \frac{t_{\mathrm{composite\_k}}}{j\omega A_n k_{\mathrm{composite}}\varepsilon_0}$$

$$= Z_{\mathrm{air\_k}} + Z_{\mathrm{composite\_k}} \qquad (2)$$

where ω is the frequency of alternating current, k is the dielectric constant, ε_0 is the permittivity of vacuum, and t is the thickness.

With the assumption that the porosity is uniform over the whole PNC, the thickness of the air and the composite in all columns are the same, respectively. ($t_{\mathrm{air\_1}} = t_{\mathrm{air\_2}} = \cdots = t_{\mathrm{air\_}n} = t_{\mathrm{air}}$, $t_{\mathrm{composite\_1}} = t_{\mathrm{composite\_2}} = \cdots = t_{\mathrm{composite\_}n} = t_{\mathrm{composite}}$)

Thus, for all k, Z_{k} is the same.

$$\frac{1}{Z_{sensor}} = \sum_{k=1}^{n} \frac{1}{Z_{\mathrm{k}}} = \frac{n}{Z_n} \qquad (3)$$

The impedance of whole sensor can be described by two components, C_{air} and $C_{\text{composite}}$, as in the following:

$$Z_{\text{sensor}} = \frac{Z_n}{n}$$

$$= \frac{1}{n}\left(\frac{t_{air}}{j\omega A_n k_{\text{air}}\varepsilon_0} + \frac{t_{composite}}{j\omega A_n k_{\text{composite}}\varepsilon_0}\right)$$

$$= \frac{t_{air}}{j\omega A k_{\text{air}}\varepsilon_0} + \frac{t_{composite}}{j\omega A k_{\text{composite}}\varepsilon_0}$$

$$= \frac{1}{j\omega C_{\text{air}}} + \frac{1}{j\omega C_{\text{composite}}} \qquad (4)$$

- HRPS with a conductive PNC

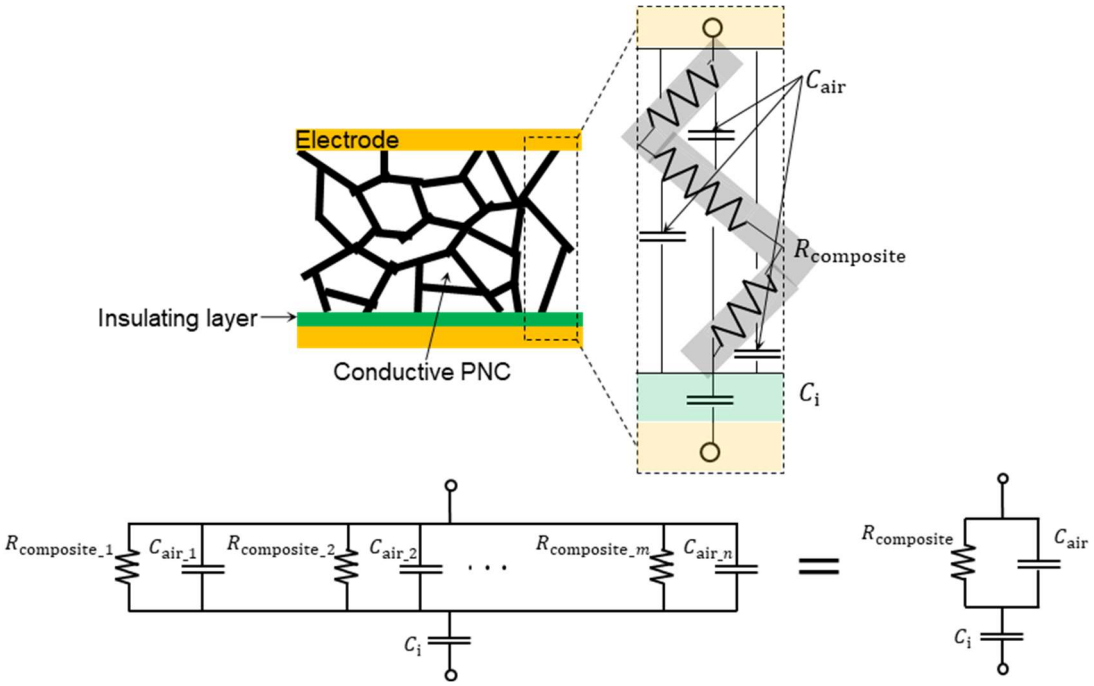

Figure SA2. Simplification of the equivalent circuit of HRPS with a conductive PNC

The high resistance of nanocomposite causes a significant voltage drop through ligaments of conductive PNC. Thus, it is assumed that the electric field is only generated vertical to the electrodes, and the resistance of the composite and the capacitance of air are arranged in parallel.

$$\frac{1}{Z_{\text{conductive PNC}}} = \sum_{k=1}^{m} \frac{1}{Z_{\text{composite\_k}}} + \sum_{i=1}^{n} \frac{1}{Z_{\text{air\_i}}} \quad (5)$$

$$\sum_{\text{i=1}}^{\text{m}} \frac{1}{Z_{\text{composite\_k}}} = \frac{1}{R_{\text{composite}}} \text{ ($R_{\text{composite}}$ is extracted from experimental measurement)} \quad (6)$$

With the assumption that the porosity is uniform over the whole PNC, for all i, the $t_{\text{air\_i}}$ are the same. ($t_{\text{air\_1}} = t_{\text{air\_2}} = \cdots = t_{\text{air\_}n} = t_{\text{air}}$)

Thus, $C_{\text{air\_1}} = C_{\text{air\_2}} = \cdots = C_{\text{air\_}n}$

$$\sum_{\text{i=1}}^{\text{n}} \frac{1}{Z_{\text{air\_i}}} = \frac{n}{Z_{\text{air\_}n}} = n\left(\frac{j\omega A_n k_{\text{air}} \varepsilon_0}{t_{\text{air}}}\right) = \frac{j\omega A k_{\text{air}} \varepsilon_0}{t_{\text{air}}} = j\omega C_{\text{air}} \quad (7)$$

Finally, we can sufficiently describe the mechanism of the HRPS using three components, $R_{\text{composite}}$, C_{air} and C_{i} as seen below:

$$Z_{\text{HRPS}} = Z_{\text{conductive PNC}} + Z_{\text{insulating layer}} = \frac{1}{\frac{1}{R_{\text{composite}}} + j\omega C_{\text{air}}} + \frac{1}{j\omega C_{\text{i}}} \quad (8)$$

B. Components in equivalent circuits

- Capacitive pressure sensor with a nonconductive PNC

The capacitance of composite and air can be defined as

$$C_{\text{composite}} = \frac{k_{\text{composite}} \cdot \varepsilon_0 \cdot A}{t_{\text{composite}}} \quad (9)$$

$$C_{\text{air}} = \frac{k_{\text{air}} \cdot \varepsilon_0 \cdot A}{t_{\text{air}}} \quad (10)$$

Considering the porosity of the PNC (φ_0), the initial thickness of the composite and air can be determined as

$$t_{\text{composite}_0} = t(1-\varphi_0) \qquad (11)$$

$$t_{\text{air}_0} = t \cdot \varphi_0 \qquad (12)$$

where t is the initial thickness of the PNC. The thickness of composite is constant as the nanocomposite is an incompressible material. ($t_{\text{composite}} = t_{\text{composite}_0}$) Additionally, compression only affects the thickness of the air. The nominal compressive strain (ϵ) is

$$\epsilon = 1 - \frac{(t_{\text{air}} + t_{\text{composite}})}{(t_{\text{air}_0} + t_{\text{composite}_0})} \qquad (13)$$

Using the Equation (11) and (12), the strain can be expressed as

$$\epsilon = \varphi_0 - \frac{t_{\text{air}}}{t} \qquad (14)$$

and the thickness of air can be expressed as

$$t_{\text{air}} = t(\varphi_0 - \epsilon) \qquad (15)$$

Substituting Equations (11) and (15) into (9) and (10), respectively, the capacitance of nanocomposite and air are described as below.

$$C_{\text{composite}} = \frac{k_{\text{composite}} \cdot \varepsilon_0 \cdot A}{\text{t}(1-\varphi_0)} \qquad (16)$$

$$C_{\text{air}} = \frac{k_{\text{air}} \cdot \varepsilon_0 \cdot A}{t(\varphi_0 - \epsilon)} \qquad (17)$$

- HRPS with a conductive PNC

From the previous derivation for nonconductive PNC, the capacitance of air is

$$C_{\text{air}} = \frac{k_{\text{air}} \cdot \varepsilon_0 \cdot A}{t(\varphi_0 - \epsilon)} \qquad (118)$$

The capacitance of insulating layer can be expressed as

$$C_{\text{i}} = \frac{k_{\text{PMMA}} \cdot \varepsilon_0 \cdot A}{t_{\text{PMMA}}} \qquad (19)$$

The resistance of the conductive PNC was extracted through experimental measurement and is

$$R_{\text{composite}} = \frac{R_0}{\varphi_0^2}(\epsilon - \varphi_0)^2 + \frac{R_0}{1000} \qquad (20)$$

C. Optimal R_0 of conductive PNC for the highest sensitivity of HRPS

For brevity, $R_{\text{composite}}$ is denoted as R from here on.

The impedances due to the resistance of PNC, capacitance of PNC, and capacitance of insulating layer are

$$Z_{\text{R}} = R \qquad (21)$$

$$Z_{\text{C}} = \frac{1}{j\omega_{\text{air}}} \qquad (22)$$

$$Z_{\text{i}} = \frac{1}{j\omega C_{\text{i}}} \qquad (23)$$

With the simplified equivalent circuit of the HRPS described in Figure 4g, the impedance of the whole HRPS can be described as

$$Z_{\text{HRPS}} = \frac{Z_{\text{R}} Z_{\text{C}}}{Z_{\text{R}} + Z_{\text{C}}} + Z_{\text{i}} = \frac{R}{1 + \omega^2 R^2 {C_{\text{air}}}^2} - \left(\frac{\omega R^2 C_{\text{air}}}{1 + \omega^2 R^2 {C_{\text{air}}}^2} + \frac{1}{\omega C_{\text{i}}}\right) j \qquad (24)$$

The reactance of the HRPS is

$$X_{\mathrm{HRPS}} = -\left(\frac{\omega R^2 C_{\mathrm{air}}}{1+\omega^2 R^2 {C_{\mathrm{air}}}^2} + \frac{1}{\omega C_{\mathrm{i}}}\right) \qquad (25)$$

The whole capacitance and normalized capacitance change of HRPS can be expressed as below:

$$C_{\mathrm{HRPS}} = -\frac{1}{\omega X_{\mathrm{HRPS}}} = \frac{C_i(1+\omega^2 R^2 {C_{\mathrm{air}}}^2)}{1+\omega^2 R^2 C_{\mathrm{air}}(C_{\mathrm{air}}+C_{\mathrm{i}})} \qquad (26)$$

$$\text{Normalized } \Delta C_{\mathrm{HRPS}} = \frac{C_{\mathrm{HRPS}}-C_{\mathrm{HRPS}_0}}{C_{\mathrm{HRPS}_0}} = \frac{(1+\omega^2 {R_0}^2 C_{air_0}(C_{air_0}+C_i))(1+\omega^2 R^2 {C_{\mathrm{air}}}^2)}{(1+\omega^2 R^2 C_{\mathrm{air}}(C_{\mathrm{air}}+C_i))(1+\omega^2 {R_0}^2 {C_{\mathrm{air}_0}}^2)} - 1 \qquad (27)$$

To get the optimal R_0 for the maximum normalized ΔC_{HRPS} at 94.7% compression of the PNC (corresponding to the maximum pressure of 50 kPa applied in our experiments),

$$\epsilon = \varphi_0 * 0.947 \qquad (28)$$

$$\frac{d(\text{Normalized } \Delta C_{\mathrm{HRPS}})}{dR_0} = 0 \qquad (29)$$

As a sidenote, $C_{\mathrm{air}} = C_{\mathrm{air}_0}\frac{\varphi_0}{\varphi_0-\epsilon}$ was used instead of $C_{\mathrm{air}} = \frac{k_{\mathrm{air}}\cdot\varepsilon_0\cdot A}{t(\varphi_0-\epsilon)}$.

Among the five solutions for $R_{0_{\mathrm{optimum}}}$, one positive real solution is

$$R_{0_{\mathrm{optimum}}} = \left(\frac{53000\left(1481080505073^{\frac{1}{2}}\left(C_{\mathrm{air}_0}(279449151900\ \ {}_{\mathrm{air}_0}+2808231050507C_{\mathrm{i}})\right)^{\frac{1}{2}}+191177519000\ \ {}_{\mathrm{air}_0}\right)}{3809(13436851900\ \ {}_{\mathrm{air}_0}{}^3\omega^2+1481080505\ \ {}_{\mathrm{i}}{C_{\mathrm{air}_0}}^2\omega^2)}\right)^{\frac{1}{2}} \qquad (30)$$

As $C_{\mathrm{i}} >> C_{\mathrm{air}}$, the terms $2794491519000C_{\mathrm{air}_0}$, $191177519000C_{\mathrm{air}_0}$ in numerator, and $134368519000{C_{\mathrm{air}_0}}^3\omega^2$ in denominator are neglected. Then, the R_0 can be simply described as

$$R_{0_{\mathrm{optimum}}} = 7.7839\ \omega^{-1}\ {C_{\mathrm{air}_0}}^{-\frac{3}{4}}\ {C_{\mathrm{i}}}^{-\frac{1}{4}} \qquad (31)$$

Section 2. Supporting figures

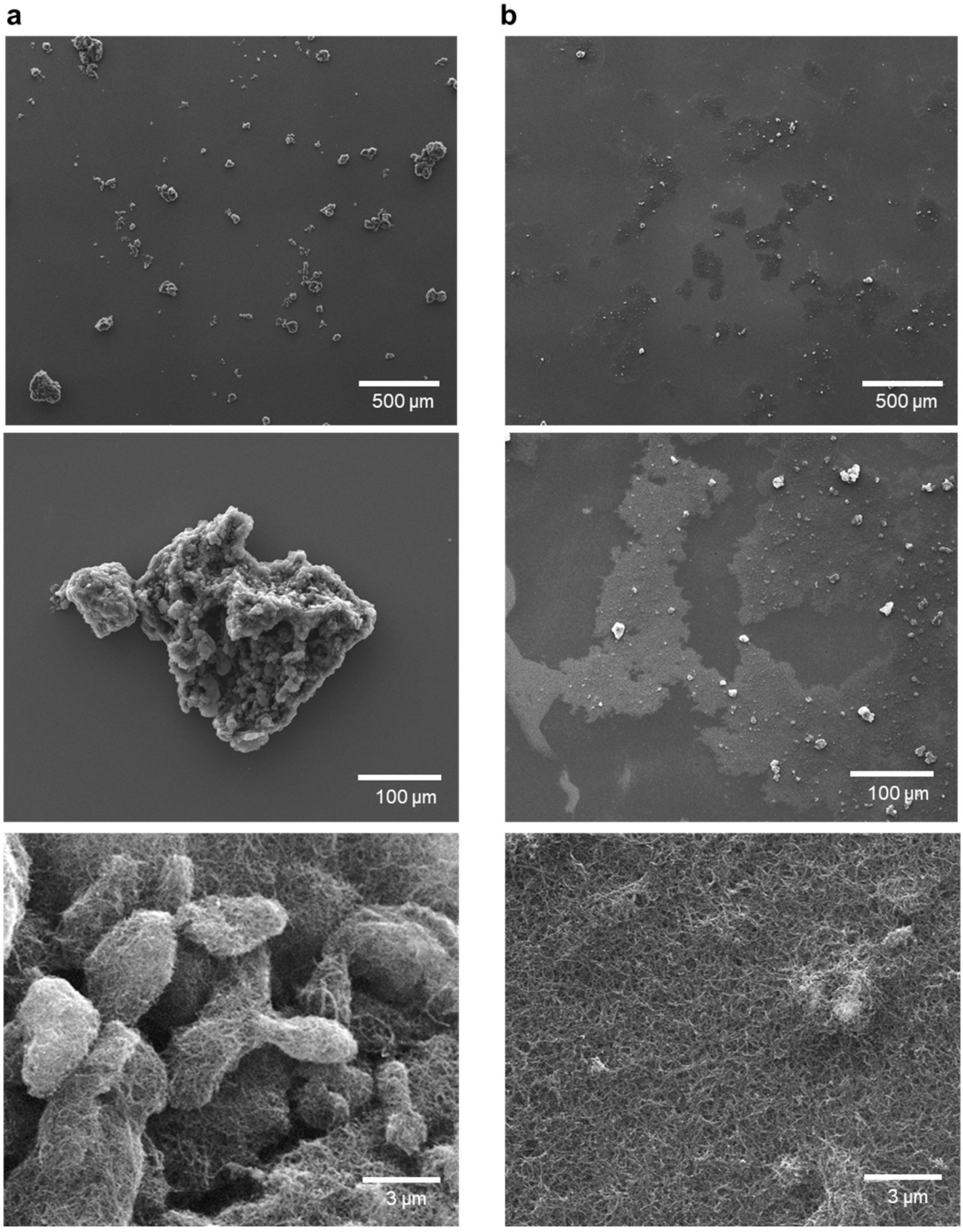

Figure S1. SEM images of CNTs on silicon wafer a) before and b) after sonication in a chloroform solution.

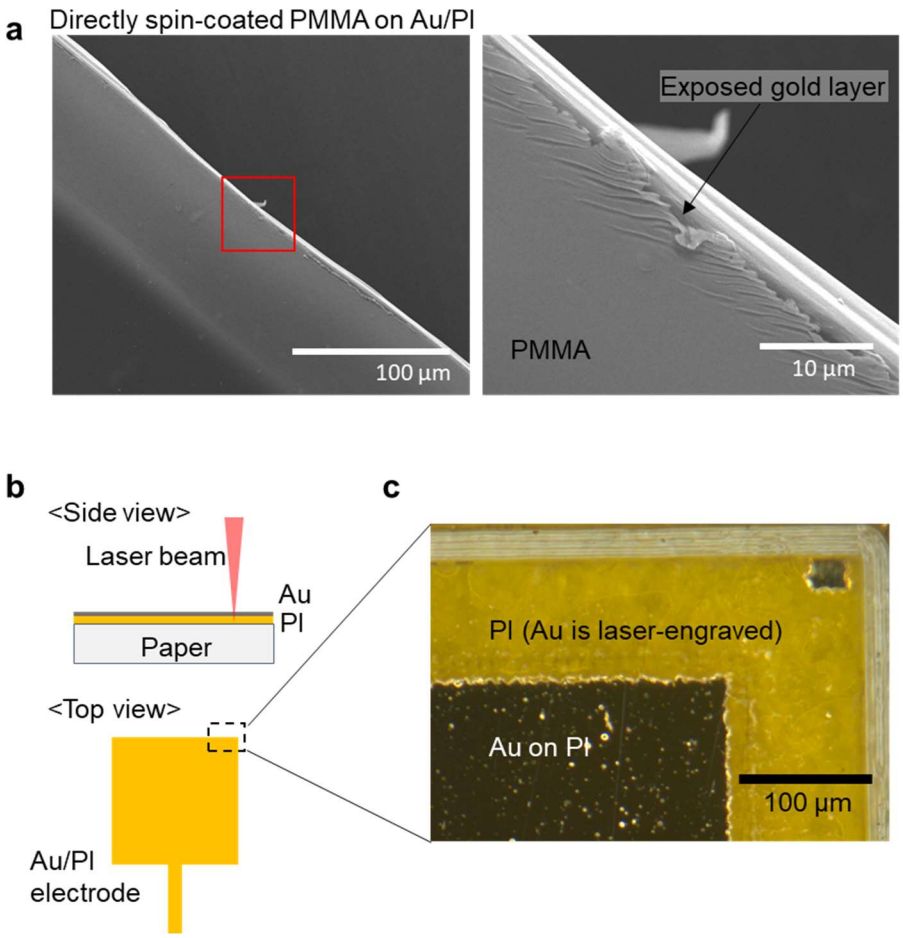

Figure S2. Fabrication of HRPS electrode with insulating PMMA layer. a) SEM images of directly spin-coated PMMA on Au/PI. PMMA does not fully cover the gold electrode all the way to the edges. To make a perfectly insulated electrode, the gold was engraved 100 µm from the edges using a laser cutter. b) Illustration of laser machining Au/PI film supported by a paper tape. c) Optical micrograph of a corner of the engraved Au/PI electrode.

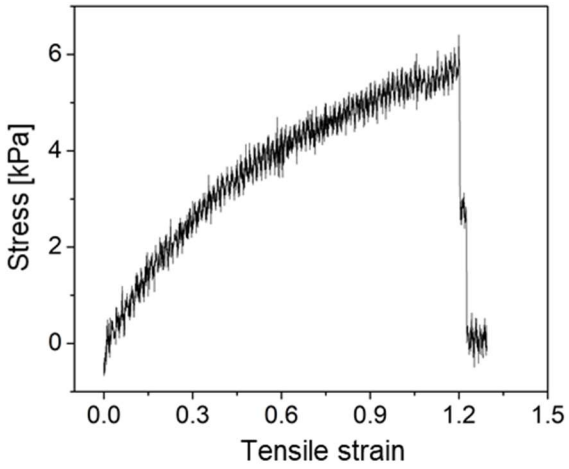

Figure S3. Uniaxial tensile test of a conductive PNC until fracture. To estimate the minimum bending radius of the PNC, maximum tensile strain was measured. The tensile strain ϵ generated under bending is $\epsilon = \frac{t}{2R}$, where t is the thickness of PNC and R is the bending radius. As the maximum strain was 1.2 and the thickness was 650 μm, the maximum bending radius was estimated to be 271 μm.

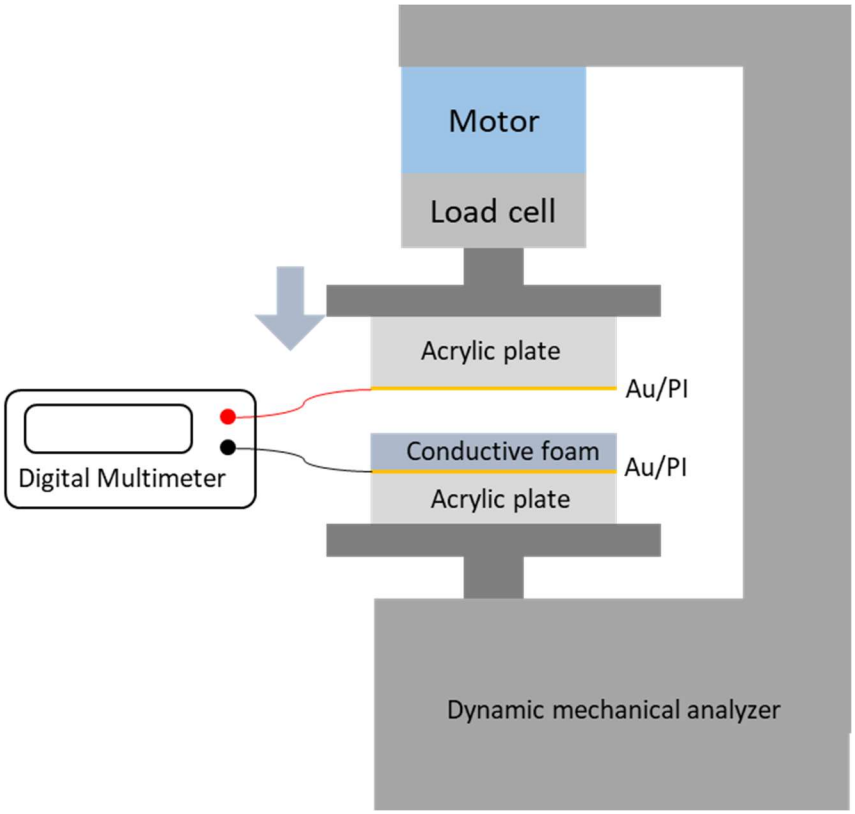

Figure S4. Illustration of experimental setup for measuring the resistance of the conductive PNC.

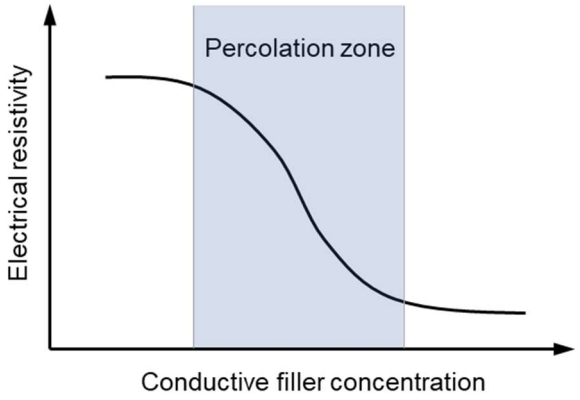

Figure S5. Typical electrical resistivity change of nanocomposite depending on the conductive filler concentration. The different slopes of the four resistance vs. compressive strain curves in Figure 2b can be understood through percolation theory. For our PNC, the percolation zone lies within 0.25 wt% to 1 wt%. The greatest piezoresistivity, i.e., the largest slope, should appear at the percolation threshold, defined as the steepest point of the percolation zone. Hence, nonmonotonic piezoresistivity (i.e. gauge factor of piezoresistive sensors) vs. doping concentration is expected and has been reported in the literature.[1, 2]

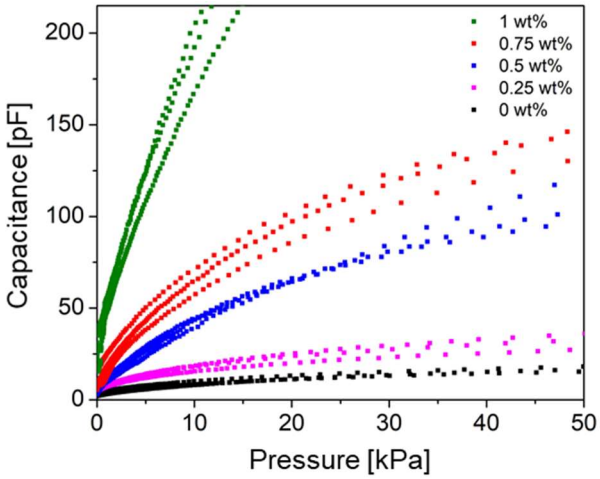

Figure S6. Capacitance change of HRPS with different amount of CNT in PNCs. Three samples were fabricated for each composition and only the middle curves of each group are plotted in Figure 2c.

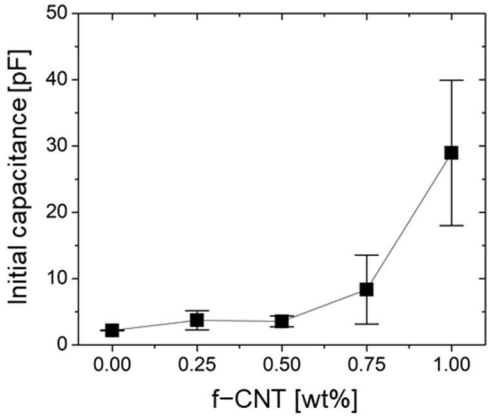

Figure S7. Initial capacitance of HRPS depending on CNT doping ratio.

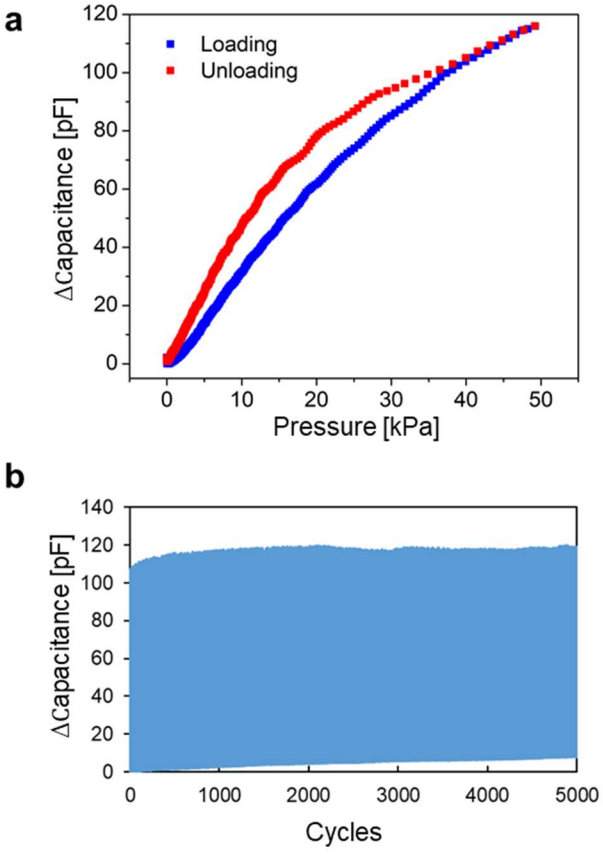

Figure S8. Loading-unloading test and cyclic test of HRPS up to 50 kPa pressure. a) The loading-unloading response of the HRPS is a typical curve for compressed porous materials with hysteresis due to the instability of the porous structure. b) A cyclic test with 50 kPa resulted in a slight increase of the baseline. This is due to irreversibly closed pores under repeated high compression.

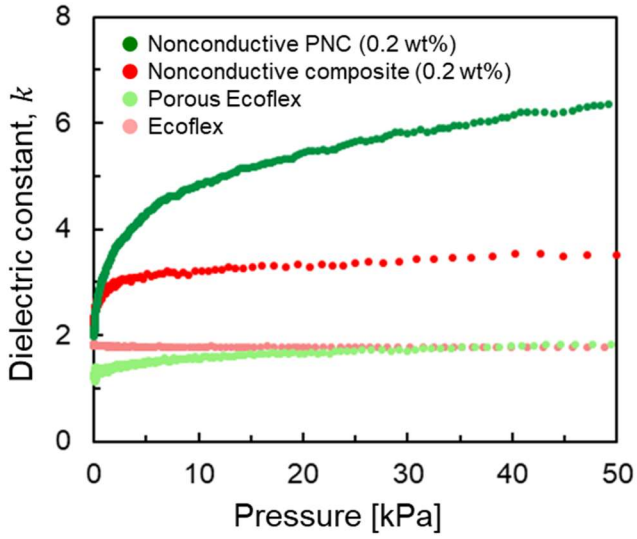

Figure S9. Measured pressure response of effective dielectric constant (*k*) of the four different dielectric materials in this study. The enhancement to dielectric constant from doping conductive fillers can be seen by comparing solid and porous Ecoflex against solid and porous nonconductive nanocomposite under large pressure. Without pressure, the dielectric constants of all four materials are similar due to the ultralow CNT doping ratio in the composites (0.2 wt%), except that the porous structures have slightly lower dielectric constants than their solid counterparts due to the air pores. However, under large pressure (e.g., 50 kPa) the dielectric constant of the solid Ecoflex remains unchanged; the dielectric constant of the porous Ecoflex approaches that of the solid Ecoflex (1.9); whereas the dielectric constants of the porous nanocomposite (6.4) becomes significantly higher than that of the solid nanocomposite (3.5), which is still higher than that of the solid Ecoflex (1.9). The different behaviors of solid vs. porous nanocomposites under pressure can be attributed to the ultrahigh porosity (86%) and the tubular morphology of the ligaments in the PNC, which ensures much denser packing of the CNT, as reported in other research.[3] Note that the dielectric constant of the solid composite increases with compression while that of the Ecoflex remains consistent. This is due to the CNT densification in the thickness direction, which is also the direction of the electrical field. This phenomenon has been reported in other nanocomposites.[4]

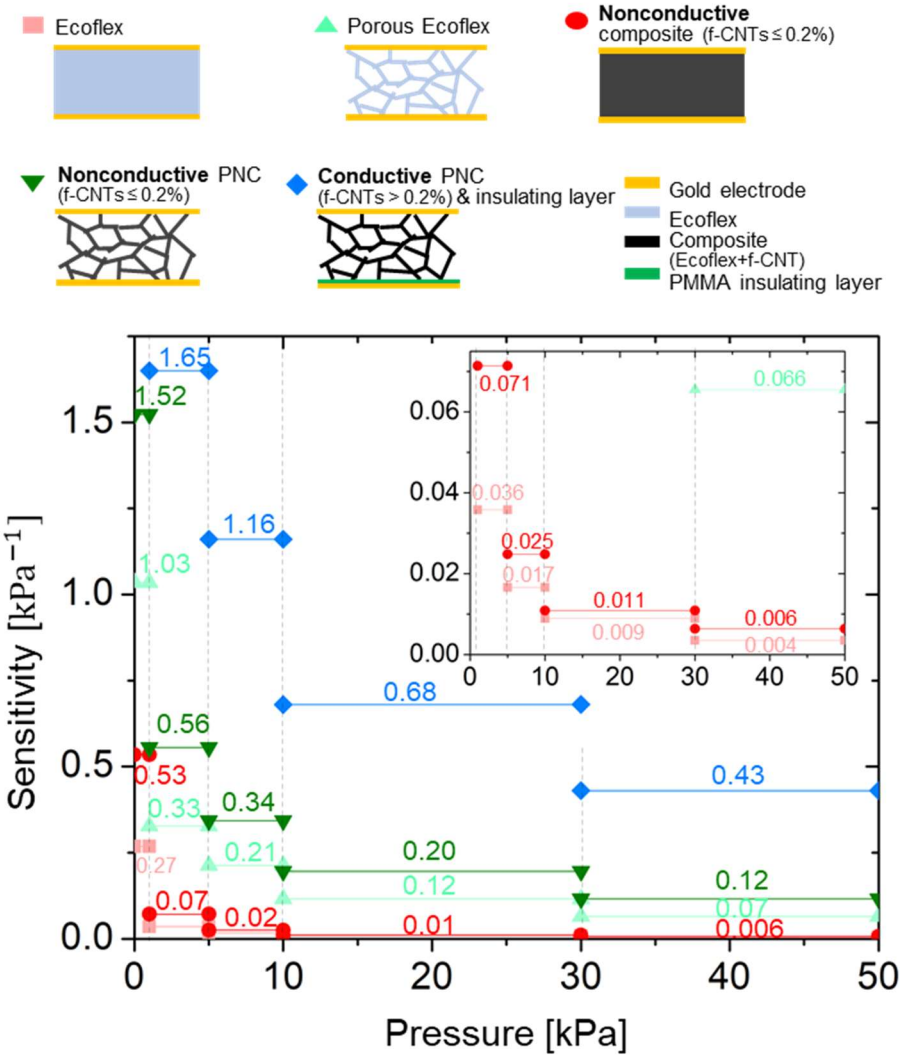

Figure S10. Sensitivity of HRPS and conventional capacitive pressure sensors in the pressure ranges of 0-1, 1-5, 5-10, 10-30, and 30-50 kPa.

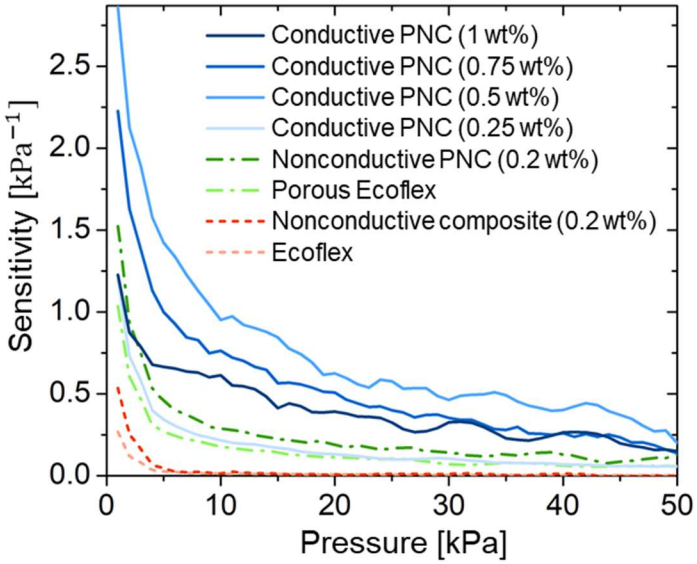

Figure S11. Absolute tangential sensitivity of HRPS with conductive PNC and conventional capacitive pressure sensors as a function of pressure.

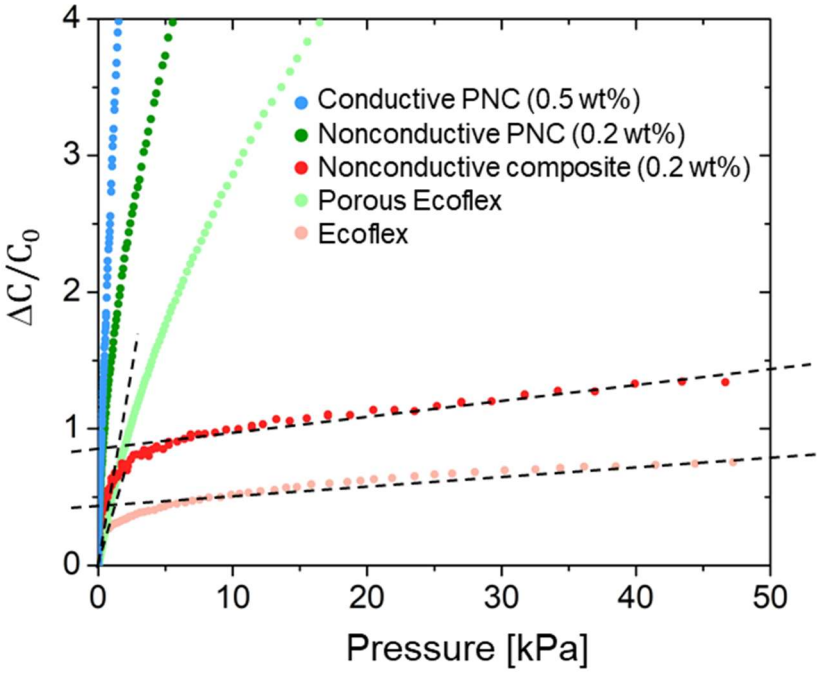

Figure S12. Relative capacitance change of HRPS and conventional capacitive pressure sensors in a y-scale smaller than Figure 3*d*. capacitive pressure sensor with solid materials (Ecoflex and nonconductive nanocomposite) show a clear bilinear response and a sharp decay in sensitivity with pressure.

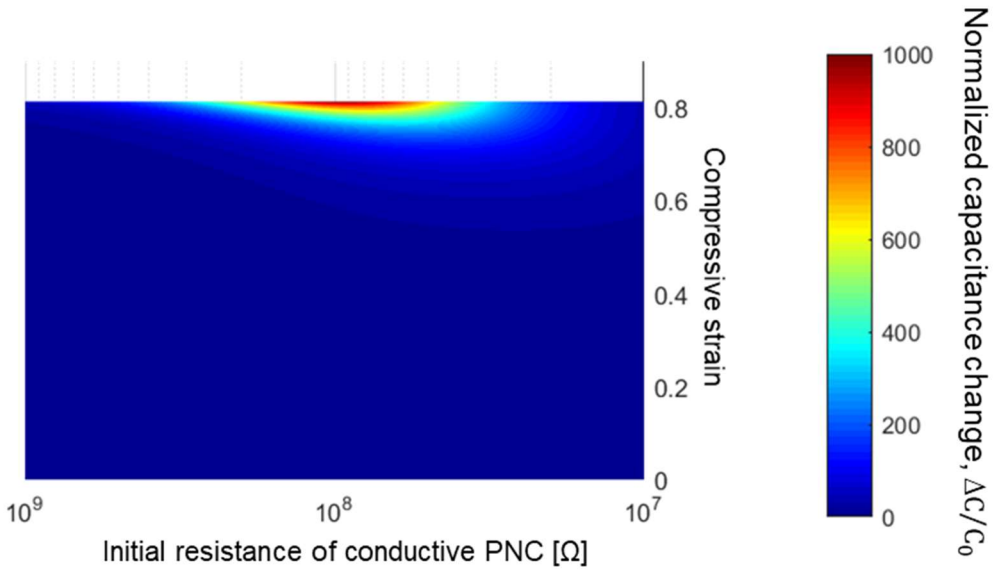

Figure S13. Analytical calculation of normalized capacitance change of HRPS depending on different R_0 of conductive PNC from 10 MΩ to 1 GΩ. An optimal resistance for sensitivity clearly exists.

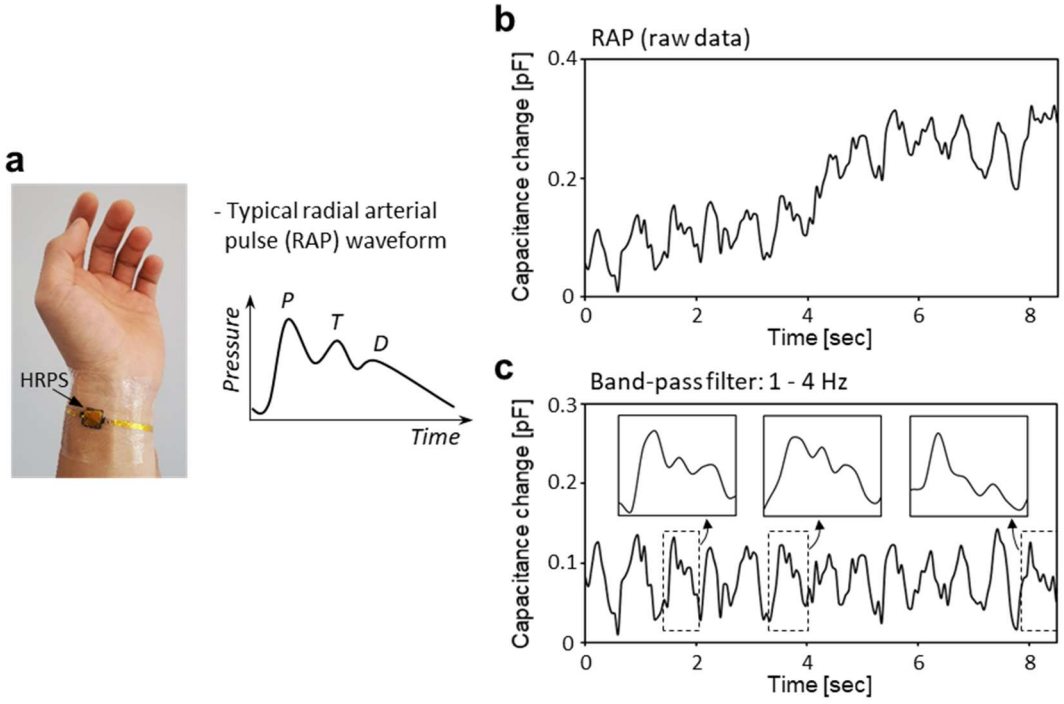

Figure S14. Demonstration of the HRPS measuring the radial arterial pulse (RAP). a) Photograph of the HRPS installed over the radial artery and a benchmark waveform of RAP. b) Raw RAP measured by the HRPS. c) Filtered RAP using a band pass filter from 1 to 4 Hz.

References

[1] M. Panahi-Sarmad, M. Noroozi, M. Abrisham, S. Eghbalinia, F. Teimoury, A. R. Bahramian, P. Dehghan, M. Sadri, V. Goodarzi, *ACS Appl. Electron. Mater.* **2020**, 2, 2318.

[2] T. Zhai, D. Li, G. Fei, H. Xia, *Compos. Part A Appl. Sci. Manuf.* **2015**, 72, 108.

[3] C. M. Tringides, N. Vachicouras, I. de Lázaro, H. Wang, A. Trouillet, B. R. Seo, A. Elosegui-Artola, F. Fallegger, Y. Shin, C. Casiraghi, *Nat. Nanotechnol.* **2021**, 1.

[4] J. Wang, J. Jiu, M. Nogi, T. Sugahara, S. Nagao, H. Koga, P. He, K. Suganuma, *Nanoscale* **2015**, 7, 2926.